ANALYSIS OF TRMM PRECIPITATION RADAR ALGORITHMS AND RAIN

OVER THE TROPICS AND SOUTHEAST TEXAS

A Thesis

by

AARON BRANDON FUNK

Submitted to the Office of Graduate and Professional Studies of
Texas A&M University
in partial fulfillment of the requirements for the degree of

MASTER OF SCIENCE

Chair of Committee,   Courtney Schumacher
Committee Members,   Shaima Nasiri
                                 Oliver Frauenfeld
Head of Department,   Ping Yang

December 2013

Major Subject: Atmospheric Sciences

ABSTRACT

The Tropical Rainfall Measuring Mission (TRMM) Precipitation Radar (PR) 2A23 algorithm classifies rain echo as stratiform or convective while the 2A25 algorithm corrects vertical profiles of radar reflectivity for attenuation and calculates rain rates associated with the attenuation-corrected reflectivity. Updates to the 2A23 algorithm for Version 7 (V7) have resulted in an increase (decrease) in the fraction of rain echo classified as convective (stratiform) compared with previous versions of the algorithm. The tropics-wide (20°N-20°S) stratiform rain fraction has decreased correspondingly, which has implications for studying the impact of convection on the large-scale circulation because of the elevated heating associated with stratiform rain. Updates to the 2A25 algorithm have resulted in changes in the rain rates derived from radar reflectivity, with convective rain over land increasing between V6 and V7. Drop size distributions (DSD) from 2A25 are compared to rainfall data collected at two ground instrument sites in southeast Texas and show that the TRMM PR is still likely underestimating heavy rain rates over land, with implications for quantifying flash flood events and model evaluations of rain rate distributions.

ACKNOWLEDGEMENTS

NOMENCLATURE

DSD   Raindrop Size Distribution

FAD   Frequency by Altitude Diagram

JAXA   Japan Aerospace Exploration Agency

MCS   Mesoscale Convective System

PIA   Path Integrated Attenuation

PR   Precipitation Radar

R   Rain Rate

TRMM   Tropical Rainfall Measuring Mission

V5   Version 5

V6   Version 6

V7   Version 7

Z   Radar Reflectivity Factor

TABLE OF CONTENTS

LIST OF FIGURES

LIST OF TABLES

1. INTRODUCTION

The Tropical Rainfall Measuring Mission (TRMM) satellite was launched in 1997 as a joint mission between the National Aeronautics and Space Administration (NASA) and the Japan Aerospace Exploration Agency (JAXA) to gather rain statistics across the tropics. To date, TRMM has produced a nearly continuous tropical rainfall dataset utilizing several onboard instruments including the TRMM Precipitation Radar (PR), a first-of-its-kind space borne K_u-band (13.8 GHz) meteorological radar based on phased array technology that gathers profiles of radar reflectivity across latitudes approximately 35°N to 35°S (Kummerow et al. 1998).

Prior to the TRMM mission, a long-term, tropics-wide, 3-D precipitation dataset did not exist. Rainfall over the tropical land sites was poorly sampled and rainfall over the tropical ocean was sampled even less. Complex field experiments studying tropical rainfall were limited spatially and temporally. One of the largest field experiments, GARP Atlantic Tropical Experiment (GATE), was centered in the tropical Atlantic ocean and covered latitudes 20°N to 10°S and longitudes 95°W to 55°E. The experiment lasted 100 days during the summer of 1974 and deployed 40 ships, 13 aircraft, and many ground instrument sites and included participation from those in over 70 countries (Kuettner 1974). However, field experiments of this size are expensive and difficult to execute. For the tropical oceans, a remote-sensing method was proposed by Griffin et al. (1978) using satellites to measure outgoing longwave radiation (OLR) to empirically estimate the amount of rainfall. The authors found that the accuracy of rainfall estimation was sometimes poor and that the derived empirical relationships used to estimate rainfall varied regionally. The authors also found that the error in rainfall estimation increased with decreasing time intervals. Further,

this method was only able to provide 2-D rainfall estimates and did not provide data in the vertical.

Precipitation is an important part of the hydrological cycle. More than two-thirds of the global rainfall occurs between 30°N-30°S (Simpson et al. 1988) and so accurate data on tropical rainfall, including information on its vertical structure, is important for many reasons. For example, latent heat produced by precipitation processes helps to drive global circulations such as the Walker and Hadley Cells (e.g., Hartmann et al. 1984, Schumacher et al. 2004) and these large-scale atmospheric circulations are responsible for transporting a significant amount of heat from the equator toward the poles making them important in the study of climate. Heating profiles vary by rain type due to the different microphysical process associated with hydrometeor production in each type and small changes in rain classifications can have impacts on the overall heating profile.

There are two main types of precipitation in the tropics: stratiform and convective (Houze 1997, Fig. 1). Dynamically, convective rain (Fig. 1a) has air converging at lower levels and diverging at upper levels with strong updrafts in between. Stratiform rain (Fig. 1d) has air converging at midlevels and diverging at lower and upper levels with weak updrafts above and weak downdrafts below the convergent layer. In regards to hydrometeor growth, convective drops primarily grow through collision and coalescence in the strong updrafts (Fig. 1b), a process at lower levels where large drops with higher terminal velocity collide and coalesce with smaller, slower drops. In stratiform rain, the weak updrafts help to slow the decent of ice particles allowing for growth by vapor deposition (Fig. 1e). Aggregation of these ice particles also helps to increase their size and the falling drops melt at the melting layer and fall as rain. A cartoon of radar reflectivity shows large domes of high reflectivity

2

values near the surface for convective rain (Fig. 1c) while stratiform rain (Fig. 1f) is shown

having a bright band, a signature of stratiform rain on radar returns. A bright band occurs

when the aggregates of ice particle, large in area, begin to melt at the 0°C level. These large,

mixed-phase particles return more energy back to the radar due to the water's higher

reflectivity at radar wavelengths relative to ice and thus rain appears more intense in these

areas.
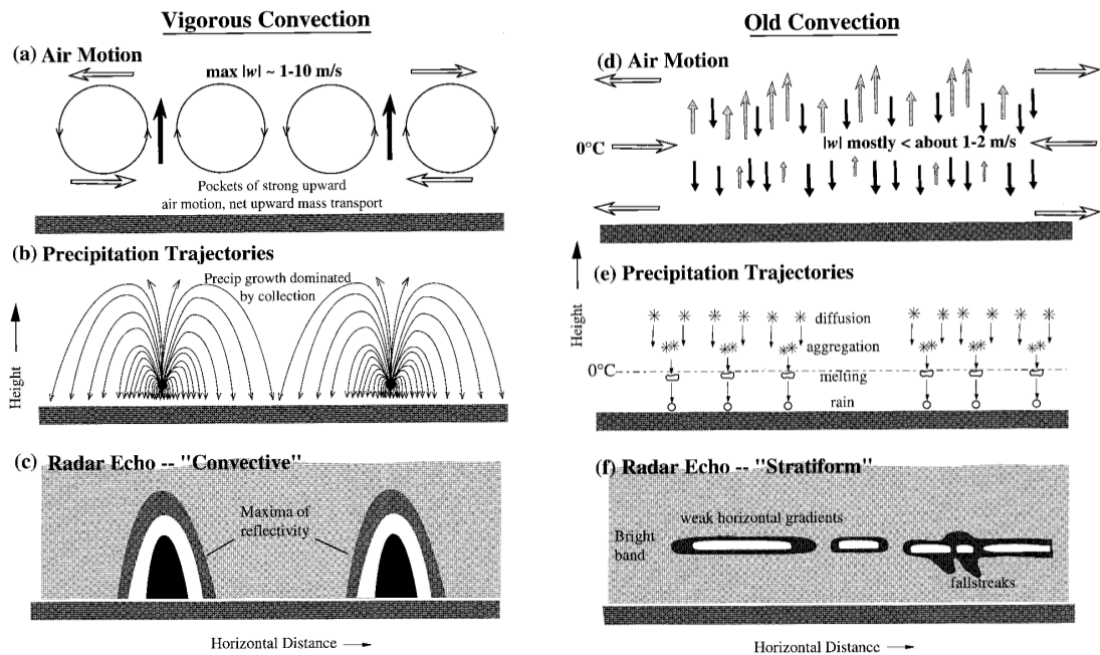
Fig. 1 –Idealized differences between stratiform ("old convective") and convective rain in the tropics. From Houze (1997).

Each type of rain produces a unique vertical latent heating profile due to the unique

microphysics responsible for generating each type of precipitation (Leary and Houze 1979,

Houze 1982). Figure 2 shows that latent heating is positive throughout the depth of the

troposphere for deep convective rain, while latent heating is positive above the 0°C level but

negative below the 0°C level in stratiform rain because of evaporation below cloud base.

3

However, most precipitation systems in the tropics are a combination of convective and stratiform rain, and Schumacher and Houze (2003) showed using an earlier version of TRMM data that approximately 40% of tropical rainfall originates in stratiform regions.
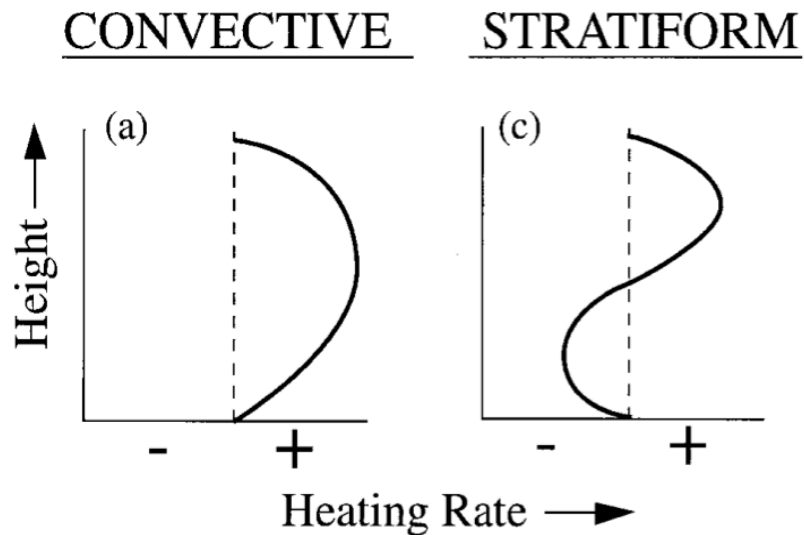
Fig. 2 – Idealized latent heating profiles in convective and stratiform rain. From Houze (1997).

Figure 3 demonstrates the sensitivity of the overall latent heating profile to changes in rainfall and stratiform rain fraction based on methods discussed in Schumacher et al. (2004). Figure 3a shows latent heating profiles for a stratiform rain fraction of 40% altering the total amount of rainfall by +/- 10%. Peak amounts of heating vary linearly. Figure 3b shows latent heating profiles for a fixed value of rainfall while the stratiform rain fraction is altered +/- 10%. Peak heating increases (decreases) and shifts upward (downward) with an increase (decrease) in stratiform rain fraction. Thus, changes in both rain amount and the type of rain producing the rain totals have implications for heating profiles and large-scale circulations

since the gradient of heating in the vertical is what drives large-scale flow (Haynes and

McIntyre 1987).
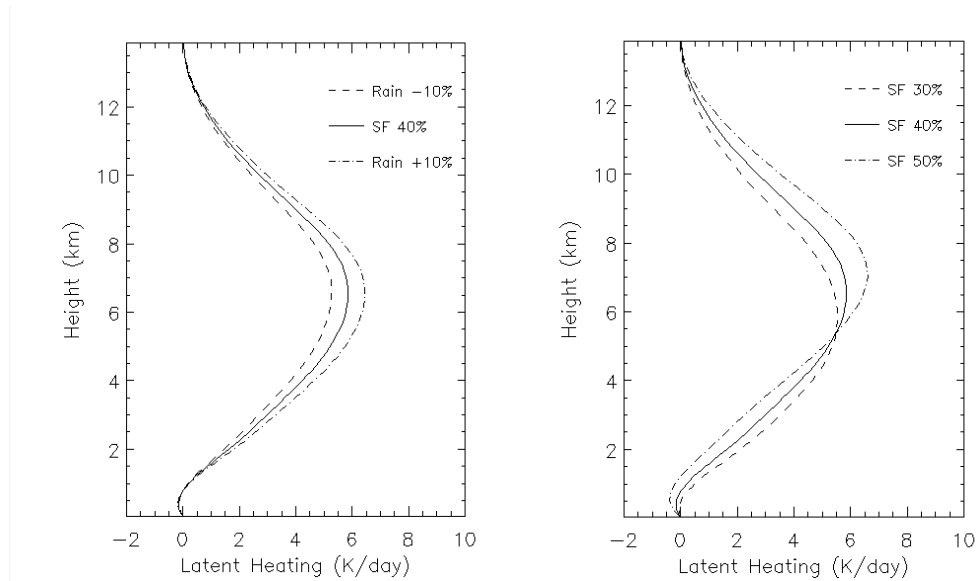
Fig. 3 – Idealized latent heating profiles based on work by Schumacher et al. (2004). Figure (a) demonstrates changes in the heating profiles based on the amount of rainfall while (b) shows sensitivity of the heating distribution to the stratiform rain fraction.

The TRMM PR has two main algorithms to determine rain type and rain totals. The

so-called 2A23 algorithm classifies radar profiles as stratiform or convective, while the so-

called 2A25 algorithm corrects radar reflectivity profiles for attenuation (i.e., the scattering

and loss of radar energy out of the path by intervening rain along the path) and calculates rain

rates from the corrected reflectivity profiles. The accurate classification of rain profiles by

the 2A23 algorithm is critical in two respects. First, as discussed above, the distinct

microphysics of each rain type generates a distinct heating profile and so correct

identification of the rain is critical to our understanding of the distribution of heating.

Further, the separation of rain into stratiform and convective plays a critical role in the

calculation of rain rates as they are calculated differently for each type. For 2A25, the

5

reflectivity and rain-rate retrievals are direct inputs into quantifying the amount of rain falling across the tropics and subtropics, as well as the associated rain rate distributions, which are important in studies of regional climate and climate change.

The purpose of this thesis is to evaluate the performance of these two algorithms. A focus will be placed on version 7 (V7) algorithms, the latest version, with some comparisons to data from version 6 (V6). Changes to the two PR algorithms for V7 include the addition of new classification criteria to 2A23 and the addition of a new drop-size distribution (DSD) model to 2A25, which is influential in the calculation of rain rates from radar reflectivity. Hundreds of studies have been published using TRMM PR data (over 500 according to a recent Web of Knowledge search), making it important to continually assess the accuracy of the PR's retrievals.

2. TRMM OVERVIEW

The TRMM satellite was planned as a 3-year mission, but in 2001, the satellite was boosted to a higher orbit from 350 km to 402 km in order to reduce atmospheric drag, conserve fuel and extend the life of the mission (Shimizu et al. 2009). The PR has a pre (post)-boost swath width of ~240 (274) km and a footprint near nadir approximately 4.3 (5) km in diameter. The boost resulted in a decrease of 1.21 dB of sensitivity with the quality of reflectivity data marginal below ~18 dBZ. Each PR scan (side-to-side) consists of 49 individual profiles. Each profile consists of bins spaced 250 meters apart from 20 km down to near the surface, the latter of which can be used to estimate rainfall at the surface for regions across the tropics and portions of the mid-latitudes.

The data collected by the PR is processed using a hierarchy of algorithms designed to quality control the data and create higher level data products appropriate for research. The algorithms are organized into three levels with each successive level providing more refined data products (TRMM PR Team 2011). Level one PR data products (1B21 and 1C21) provide radar-received power and radar reflectivity factor without corrections. Level two products (2A21, 2A23, and 2A25) provide path-integrated attenuation (PIA) based on the surface reference technique (SRT), rain types, and the attenuation-corrected radar reflectivity factor and retrieved rain rates, respectively. Level three products (3A25 and 3A26) provide gridded time-averaged data (e.g., rain rates). The algorithms have undergone several updates since the launch in 1997. TRMM's initial operational Version 4 (V4) algorithms were updated to Version 5 (V5) in 1999 and V6 in 2004. In July 2011, the reprocessing of TRMM data was initiated to generate a new V7 dataset.

2.1 2A23 Algorithm Description

The 2A23 algorithm's principle task is to classify individual PR rain pixels as either stratiform or convective (Awaka et al. 1997, 2007, 2009). The algorithm employs two independent classification methods (vertical and horizontal) and each method produces a stratiform or convective classification for each raining pixel. In the case that either method cannot classify a raining pixel as stratiform or convective, the respective method classifies the pixel as 'other'. A single, final merged classification is assigned to each raining pixel based on the classifications produced by the independent vertical and horizontal methods. Overall, 2A23 classifies raining pixels as one of 33 types (11 stratiform, 18 convective, and 4 other; Table 1). Figure 4 shows a diagram illustrating a simplified flow of the 2A23 algorithm and is described in more detail in the following paragraphs.
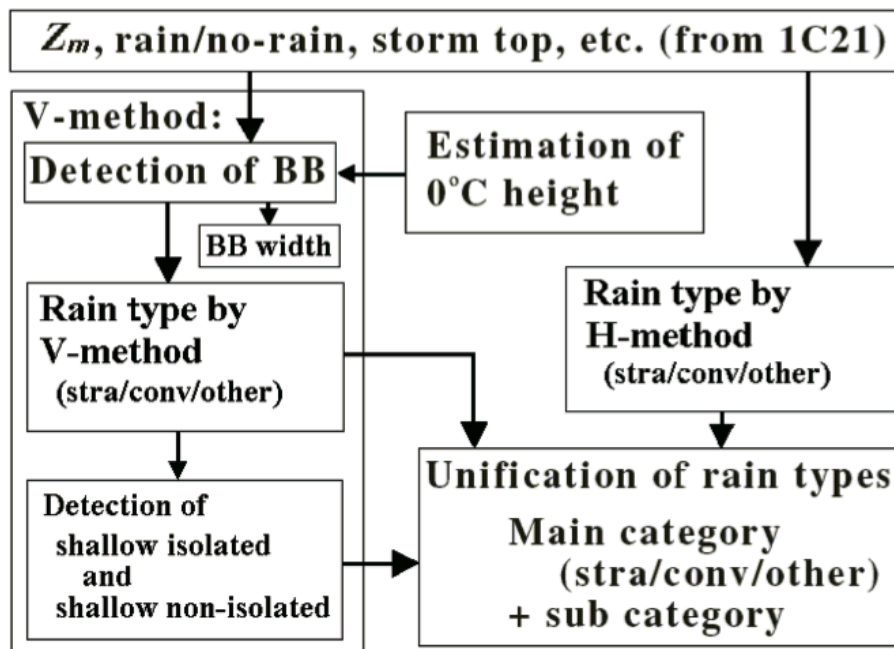
Fig. 4 – A flowchart for the basic operation of the 2A23 V6 algorithm. Awaka et al. (2009).

The 2A23 algorithm (Fig. 4) utilizes several variables from the level 1 algorithm 1C21 with the most important being the uncorrected radar reflectivity profiles and storm height information. The 2A23 algorithm first employs the vertical classification method, which attempts to identify a bright band in the reflectivity profile. It does this by examining the reflectivity values in a vertical band surrounding the climatological melting level for the profile's location. If a bright band is detected or the reflectivity values at low levels do not exceed a threshold of 40 dBZ, the vertical method classifies the profile as stratiform. If a bright band is not detected and the reflectivity values at low levels are strong or the profile is shallow isolated, the profile is classified as convective. If the profile appears as a cloud with only reflectivity values above the 0°C level or is noise, the vertical method classifies the profile as "other".

The 2A23 algorithm then employs the horizontal classification method. This method examines the rain region 1 km below the estimated 0°C level and uses a separation technique based on Steiner et al. (1995) to identify convective cells in the horizontal reflectivity field based on a peakedness criterion. Echoes from bright bands identified by the vertical method are excluded from the horizontal reflectivity field because it could contaminate the data, resulting in the identification of stratiform pixels as convective. Any pixel not identified as convective by the horizontal method is then assigned a stratiform classification.

A definition of shallow rain is also included in the 2A23 algorithm. In the determination of the vertical classification, the 2A23 algorithm detects whether a pixel is shallow or non-shallow. A shallow pixel will have rain no higher than 1.5 km below the climatological melting level. If the pixel is isolated and separated from non-shallow pixels or

9

adjacent only to other shallow pixels, it is further classified as shallow isolated. Shallow

pixels that are not shallow isolated are considered to be shallow non-isolated.

The 2A23 algorithm assigns each raining pixel a final single classification into one of

the three types (stratiform, convective, or other) based on the vertical and horizontal

classifications. This is done through the use of a three-digit number such that numbers of the

form 1xx, 2xx, and 3xx denote stratiform, convective and "other", respectively, as the final,

merged classification. Numbers further away from x00 indicate greater uncertainty in the

classification. Overall, the total number of rain types increased from 25 in 2A23 V6 to 33 in

2A23 V7. See section 3 for further information on individual rain types and information on

changes between 2A23 V6 and V7.

Examples of stratiform and convective rain as detected by the TRMM PR can be seen

in Fig. 5. Both horizontal cross sections show echo form the 2 km level. White columns in

the vertical cross sections highlight PR profiles of the relevant type (e.g., type 100 for Fig.

5b). PR profiles classified as type 100 by the 2A23 algorithm (Figs. 5a and b) have strong

bright bands and therefore confidence in the classification as stratiform is high. The highest

levels of echo in the vertical cross section (Fig. 5b) are moderate and appear just above the 4

km level. This is the stratiform bright band. PR profiles classified as type 200 by the 2A23

algorithm (Figs. 5c and d) show deep convection with reflectivity values near 50 dBZ. The

echo extends to near 10 km and the heaviest rain can be seen closest to the surface.
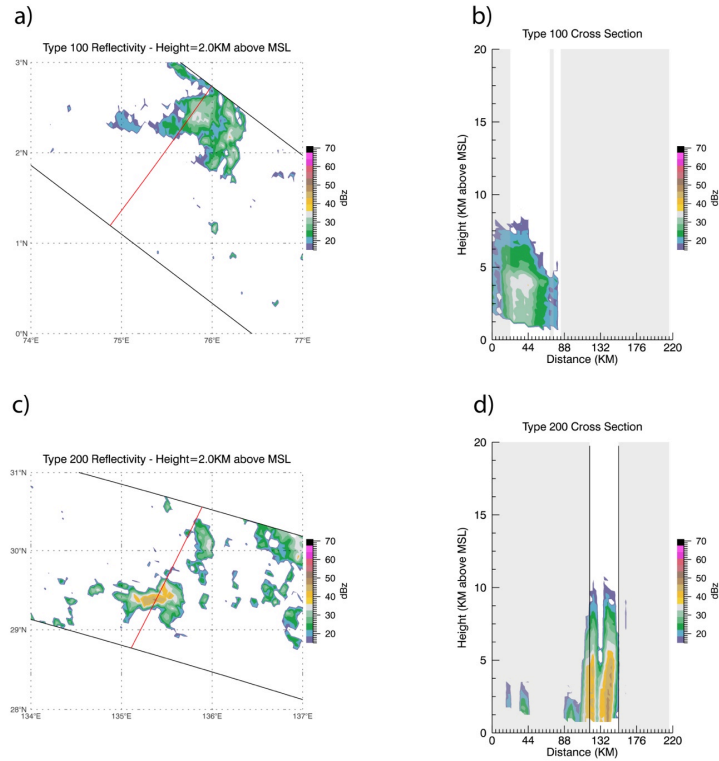
Fig. 5 – Paired horizontal and vertical cross sections of TRMM PR attenuation-corrected reflectivity data. a) and b) show type 100 stratiform data and c) and d) show type 200 convective data. Horizontal cross section data comes from the 2 km level. Red line indicates location of vertical cross section. White areas in vertical cross section identify PR profiles classified as relevant type (e.g., type 100 in b) while gray areas indicate profiles of other types. Each TRMM PR scan contains 49 profiles side-to-side.

2.2 2A25 Algorithm Description

The PR is limited by the constraints of operation in space in terms of footprint resolution and wavelength. To optimize both, you would need a large antenna, which isn't feasible in space. With a fixed antenna size there is a compromise between resolution and wavelength. While the PR operates at a relatively low altitude (350 km pre-boost, 400 km post-boost), its footprint at nadir (4.3 km pre-boost, 5 km post-boost) is still large in relation to a typical convective cell. Thus, the non-uniform distribution of rain within the radar beam is a concern. The PR's wavelength (Ku-band) also suffers from attenuation in moderate to

11

heavy rain. Because of this, profiles of radar reflectivity from space borne precipitation radars must be corrected for attenuation (Meneghini et al. 1983). The 2A25 algorithm is responsible for the correction of PR profiles of reflectivity and the calculation of rain rates from corrected values of reflectivity. The 2A25 algorithm also attempts to mitigate issues related to non-uniform beam filling (NUBF) or the inhomogeneous appearance of precipitation within a radar volume. The attenuation and NUBF issues, among others, can lead to biases in estimates of rain rate.

The power returned to the PR from precipitation can be heavily attenuated owing to intervening precipitation between the precipitation of interest and the radar, cloud liquid water, water vapor and molecular oxygen (Iguchi et al. 2009). In 1954, Hitschfeld and Bordan (H-B) presented a method for the correction of attenuated values of radar reflectivity. The technique involves directly calculating the radar energy scattered out of the path by intervening rain and works particularly well in light rain. However, the solution can be unstable in moderate to heavy rain where attenuation becomes large.

Meneghini et al. (1983, 2000) proposed an alternate solution to estimate PIA. The SRT compares previously measured normalized radar cross sections of the surface measured in clear sky conditions with normalized radar cross sections measured with precipitation present in order to estimate PIA. The method is complicated in that it is sensitive to location, surface type and, in the case of the PR, the incidence angle of the PR beam. However, SRT works best in areas of moderate to heavy rain where the attenuation is larger than the variability of the normalized radar cross sections of the surface.

For the 2A25 algorithm, the complementary H-B and SRT methods were combined to create a hybrid method for the attenuation-correction problem (Iguchi et al. 2000). The PIA

in 2A25 V7 is then estimated using a maximum likelihood method to blend results from the two methods assuming both methods provide useable results (e.g., rain is not too light or heavy so that both methods produce a solution) (Iguchi et al. 2009).

A power law relationship (k-Z) developed from the attenuation correction procedure is used to relate specific attenuation to radar reflectivity ($k=\alpha Z^{\beta}$ with $\alpha=\varepsilon\alpha_0$). For the 2A25 algorithm, epsilon was introduced as a factor that can be used to adjust α_0 in order to find a PIA from the H-B solution that matches the PIA estimate given by the SRT. Adjusting epsilon provides a stable solution to the attenuation correction problem. Further, an adjustment to epsilon, which has a nominal value of 1, can be seen as an adjustment to the DSD model used in converting reflectivity values to rain rate (Kozu et al. 2009a). The relationship between epsilon and the DSD model parameters in 2A25 are addressed explicitly in Kozu et al. (2009a). A decrease in α ($\varepsilon < 1.0$) means more large drops are included in the DSD than initially assumed, while an increase in α ($\varepsilon > 1.0$) means more small drops are included in the DSD than initially assumed. Based on changes to α, another power law relationship, the reflectivity-rain rate relationship ($Z = aR^{b}$), is modified since the Z-R relationship and k-Z relationship are related via the DSD. An adjustment to α can be viewed as an adjustment of the DSD (Kozu et al. 2009a).

The 2A25 algorithm utilizes two DSD models and separate relationships for stratiform and convective rain in order to increase accuracy of the rain rate estimates. The DSD models for stratiform and convective rain are derived from a DSD model created using tropical Z-R relationships found in literature (Kozu et al. 2009b).

Fig. 6 shows a simplified flow diagram for the 2A25 algorithm from Iguchi et al. (2009). The most important input data to 2A25 is shown including uncorrected reflectivity

13

values from 1C21, PIA estimates produced by the 2A21 SRT algorithm, as well as rain type

and the estimated 0°C level from the 2A23 algorithm. Rain type and melting layer

information from 2A23 is used to create an initial profile for the k-Z relationship as the

parameters of the k-Z relationship depend on the DSD, phase of precipitation particles in the

profile, temperature, etc. This is not explicitly known and so a model is constructed to

initialize a k-Z relationship. Adjustments are made to epsilon, if necessary, to establish a

stable H-B solution. Adjustments to epsilon result in adjustments to the Z-R relationship. The

Z-R relationship is then used to calculate the estimated rain rates. This implies that "choices"

made by the 2A25 algorithm during attenuation correction resulting in adjustments to the

stratiform and convective DSD models are important in the estimation of rain rates.

Rain Echo: $Z_m(r_i)$ (1C21) | PIA Estimate: $\Delta\sigma^0$ (2A21) | Rain Type (2A23) | 0⁰C Height (2A23)

$\zeta(r_i)$ ← Profile of k-Ze Relation

ζ Adjustment

Attenuation Correction ← H-B Attenuation Estimates with Adjusted ζ

$Z_e(r_i)$ | Z_e-R Adjustment

Ze to R Conversion ← Profile of Z_e-R Relation

$R(r_i)$
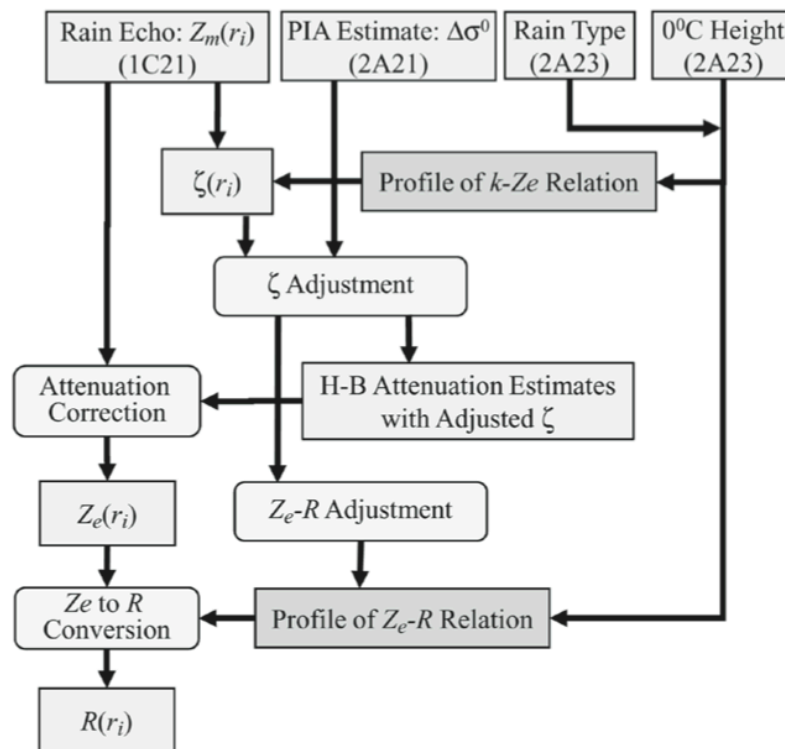
Fig. 6 – A flowchart for the basic operation of the 2A25 algorithm. Iguchi et al. (2009).

14

3. PR RAIN TYPE ALGORITHM 2A23[*]

As described in section 2.1, the TRMM 2A23 algorithm's principle task is to classify radar retrievals into one of three types on a per-pixel basis: stratiform, convective, and other. Important applications of the 2A23 algorithm include the characterization of convective and stratiform rain across the tropics (e.g., Schumacher and Houze 2003b) and the estimation of diabatic heating and drying profiles associated with convection (e.g., Shige et al. 2007, 2008). This section examines some of the changes made to the 2A23 algorithm for V7 and highlights important changes in the resulting 2A23 product. Particular emphasis will be placed on the shallow non-isolated rain category and the PR-observed changes to the tropics-wide stratiform rain fraction.

Two years of 2A23 rain types were used in this study including one preboost year (June 1999 through May 2000) and one postboost year (2008). A pixel-by-pixel comparison between 2A23 V6 data and V7 data was completed in order to find changes in rain type owing to updates made to the algorithm. Only occurrences of pixels with a corresponding 2A23 "rainFlag" value of greater than or equal to 20 are considered for this study, because they are "rain certain"; this represents the highest level of confidence, as noted in the PR manual.

---

[*]Reprinted with permission from "Analysis of Rain Classifications over the Tropics by Version 7 of the TRMM PR 2A23 Algorithm" by A. Funk, C. Schumacher and J. Awaka, 2013. *Journal of the Meteorological Society of Japan*, 91, 257-272, Copyright 2013 by Meteorological Society of Japan.

Table 1. TRMM 2A23 V7 and V6 rain-type classifications and pixel count data for June 1999 through May 2000 and all of 2008 (35°N-35°S). The "Type" column shows types 1xx (stratiform), 2xx (convective), and 3xx (other). The "Vertical" and "Horizontal" columns provide the premerged rain-type classifications. The "pixel count" column presents the number of rain-certain pixels ("rainFlag" ≥ 20). The "%" column provides percentages of all rain-certain pixels. Asterisks denote types newly introduced for 2A23 V7. Notes are Bright Band (BB), High Storm Height (HSH), Shallow Non-Isolated (SH), Shallow Isolated (SI) and Small Rain Cell (SRC).

Type	Vertical	Horizontal	Notes	V6 Pixel Count	V6 %	V7 Pixel Count	V7 %
100	Strat	Strat	BB	5.32E7	28.55	4.97E7	27.26
105*	Strat	Strat	BB, HSH	N/A	N/A	1812	< 0.01
110	Strat	Other	BB	194	< 0.01	49	< 0.01
115*	Strat	Other	BB, HSH	N/A	N/A	0	0.00
120	Other	Strat		5.24E7	28.13	5.31E7	29.13
130	Strat	Conv	BB	5.22E6	2.80	4.05E6	2.22
135*	Strat	Conv	BB, HSH	N/A	N/A	529	< 0.01
140	Other	Strat		7.93E6	4.26	4.90E6	2.69
152	Other	Strat	SH	1.69E7	9.09	8.51E6	4.67
160	Other	Strat		7.31E6	3.92	6.54E6	3.59
170	Other	Strat		3.12E6	1.67	3.15E6	1.73
All Strat				9.71E7	78.44	8.47E7	71.29
200	Conv	Conv		4.24E6	2.28	4.45E6	2.44
210	Other	Conv		1.82E7	9.76	1.78E7	9.74
220	Conv	Other		622	< 0.01	433	< 0.01
230	Strat	Conv	BB	0	0.00	54583	0.03
235*	Other	Strat	HSH	N/A	N/A	1.08E5	0.06
237*	Other	Strat	SRC	N/A	N/A	3.96E6	2.17
240	Conv	Strat		1.77E5	0.10	2.50E5	0.14
251	Conv	Conv	SI	17271	0.01	37995	0.02
252	Conv	Conv	SH	92563	0.05	1.27E5	0.07
261	Conv	Other	SI	0	0.00	0	0.00
262	Conv	Other	SH	0	0.00	0	0.00
271	Other	Conv	SI	7.61E5	0.41	9.84E5	0.54
272	Other	Conv	SH	2.23E6	1.20	2.33E6	1.28
281	Conv	Strat	SI	7	< 0.01	30	< 0.01
282	Conv	Strat	SH	177	< 0.01	227	< 0.01
291	Other	Strat	SI	1.07E7	5.74	1.12E7	6.16
292*	Other	Strat	SH	N/A	N/A	7.53E6	4.13
297*	Other	Strat	SH, SRC	N/A	N/A	98367	0.05
All Conv				3.57E7	19.54	4.76E7	26.83
300	Other	Other	Noise/Cloud	3.56E6	1.91	3.17E6	1.74
311*	Other	Other	SI	N/A	N/A	453	< 0.01
312	Other	Other	SH	6	< 0.01	6	< 0.01
313	Other	Other	SI if sidelobe clutter not rejected	2.21E5	0.12	2.63E5	0.14

3.1 2A23 V7 Changes

This subsection will not describe all changes to 2A23 for V7 but instead will highlight only a few key changes. Please refer to the V7 PR manual (TRMM PR Team 2011) for a more comprehensive list of changes in 2A23 V7. Descriptions and statistics of 2A23 V6 and V7 rain types for rain between 35°N and 35°S are listed in Table 1. A total of eight new rain types were added in 2A23 V7.

Through TRMM algorithm updates, efforts have been made to better distinguish between deep and shallow convective pixels, two modes of convection that are especially important over the tropical oceans (Short and Nakamura 2000). To further these efforts, two new concepts were introduced in 2A23 V7: small rain cells and "randomly" appearing shallow non-isolated pixels. A small rain cell is a rain cell that consists of only one isolated pixel or two adjacent isolated pixels. Small rain cell pixels are automatically regarded as being convective in 2A23 V7, and this concept is applied in two new types: 237 and 297. Table 1 indicates that type 237 accounts for 2.17% of all rain-certain pixels, whereas 297 accounts for only 0.05% of all rain-certain pixels for the examined two-year period. It should be noted that the majority of the pixels in type 237, a convective rain type, were previously classified as stratiform by 2A23 V6. More information on pixel-by-pixel type changes between V6 and V7 can be found in section 3.2.

"Randomly" appearing shallow non-isolated pixels occur within a single PR scan (i.e., a single sweep of the radar beam in a direction perpendicular to the satellite's motion). Three or less non-contiguous shallow non-isolated pixels in one scan will be counted as having appeared "randomly" and will be classified as convective in 2A23 V7. Two new convective shallow non-isolated types appear in 2A23 V7: type 292 and type 297. Note that

type 297 is also a small rain cell type. Type 292 accounts for 4.13% of rain-certain pixels for the two years examined, which is the highest percentage of new V7 rain types. The majority of these pixels were previously classified as stratiform type 152 (see section 3.2).

A third new concept introduced in 2A23 V7 is that of high storm height. High storm height is determined internally by 2A23, with the aid of data from the 1B21 and 1C21 algorithms. The 2A23 algorithm first checks that the storm top height calculated by 1B21 is greater than or equal to 12 km for the pixel being examined. If this is the case, reflectivity data from 1C21 is examined to find the highest (in altitude) bin containing real rain using methods unique to 2A23 V7. If the highest bin containing rain exceeds 15 km, the pixel is labeled as having a high storm height. Four new high storm height types appear in 2A23 V7: 105, 115, 135, and 235. Together, these account for roughly 0.06% of the rain-certain pixel count. Further discussion of the new rain types and their reflectivity distributions with height can be found in section 3.2.

3.2 Reflectivity Distributions

Frequency by altitude diagrams (FADs) provide a useful way of analyzing radar retrievals, because they can reveal features that help in differentiating between rain types, and therefore between the physical processes responsible for rain (Yuter and Houze 1995, Boccippio et al. 2005). FADs for a subset of 2A23 V7 rain types were created using 2A25 attenuation-corrected reflectivity values to illustrate the distribution of reflectivity with height (Fig. 7). As with Table 1, the same two years of data were used for the analysis, including one preboost year (June 1999 through May 2000) and one postboost year (2008). The rows of figures, beginning at the top of Fig. 7, illustrate stratiform, convective, shallow

isolated, shallow non-isolated, and anvil FADs. For the purposes of this paper, "anvil" describes pixels with radar echo aloft and little to no echo near the surface. The confidence in the accuracy of the FADs' classifications in Fig. 7 decreases from the leftmost figure to the rightmost figure. The lines in each FAD represent a 10% quantile ranging from 10% to 90%, with the median line appearing solid. It should be noted that Fig. 7 includes reflectivity values below the PR's nominal sensitivity threshold of 18 dBZ; therefore, care must be taken when studying the reflectivity distributions.

Characteristics of the stratiform FADs (Figs. 7a-c) include wider reflectivity distributions at low levels (where rain is falling below cloud base) compared with weaker and narrower reflectivity distributions above the 0°C level (where hydrometeor growth is occurring). The tapered distributions aloft suggest weak vertical velocities and homogenous microphysical growth processes (i.e., vapor deposition). As the confidence in the classification is the highest for the figure on the left, a strong bright band is evident in type 100, which the 2A23 algorithm detects to classify some pixels as stratiform. Table 1 (and the upper right corner of the FAD) indicates that type 100 accounts for 27.26% of rain-certain pixels. Type 120 does not exhibit as clear a bright band, likely due in part to scans off nadir (Awaka et al. 2009), and accounts for 29.13% of rain- certain pixels observed by the PR. Type 130 shares the narrow range of reflectivity values at upper levels with the previously noted stratiform types and exhibits a moderate bright band, but it exhibits higher reflectivity values near the surface (cf. median values of ~25 dBZ for types 100 and 120 with ~35 dBZ for type 130) and accounts for 2.22% of rain-certain pixels. The higher reflectivity values at low levels in type 130 may also be due in part to fall streaks (i.e., elongated reflectivity

19

maxima extending downward from the bright band that are associated with remnants of deep

convective cells or overturning from cooling in the melting layer, Yuter and Houze 1997).
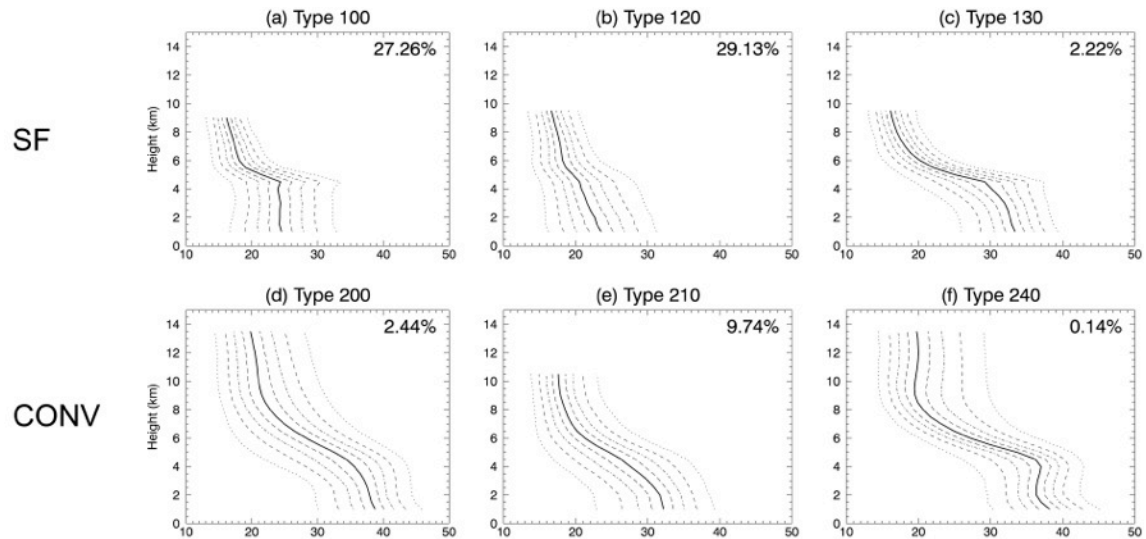
Fig. 7 - Frequency by altitude diagrams of TRMM PR 2A25-corrected reflectivity (June 1999-May 2000, 2008; 35°N-35°S) for V7. The dark line represents the median, with each line representing a 10% quantile from 10% to 90%. The percentages represent proportions of all rain-certain pixels. Row labels indicate stratiform, convective, shallow isolated, shallow non-isolated, and anvil types.
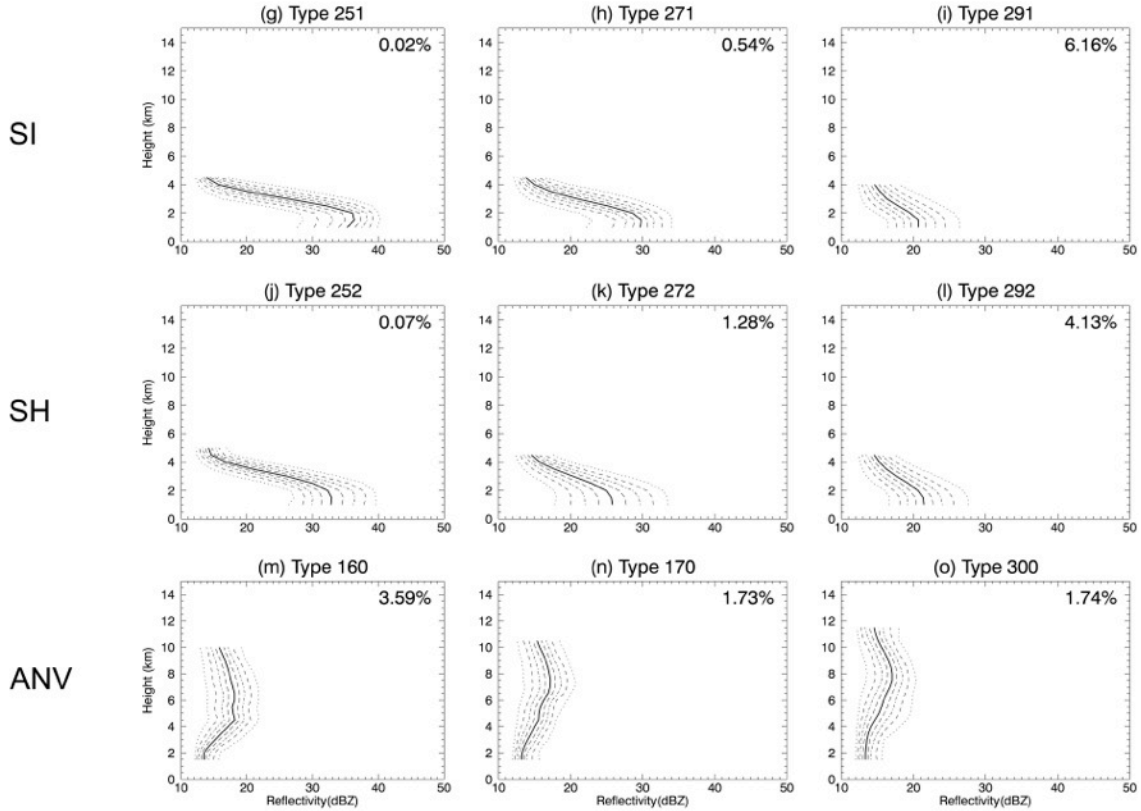
Fig. 7 - Continued

Convective reflectivity FADs (Figs. 7d-f) are characterized by higher reflectivity values at lower levels (e.g., median values up to 39 dBZ) and wider reflectivity distributions above the melting level compared with the stratiform reflectivity FADs. The wider distributions suggest stronger vertical motions and more heterogeneous microphysical growth processes. Type 200, the FAD on the left with the highest confidence, includes pixels with vigorous convection that are more likely to occur over land (not shown). Type 210, in comparison, is more likely to occur over the ocean and exhibits both lower reflectivity values and lower storm heights. Rain types 200 and 210 represent 2.44% and 9.74% of rain-certain pixels, respectively. Type 240 exhibits a possible bright band but has high near-surface

21

reflectivity values and a wide reflectivity distribution at upper levels. Type 240 accounts for only 0.14% of rain-certain pixels.

The third and fourth rows of Fig. 7 illustrate shallow isolated and shallow non-isolated FADs, respectively. Each row presents a progression of very similar reflectivity distributions with echo tops less than 5 km and a strong increase of reflectivity values toward the surface. Warm-rain processes (i.e., collision-coalescence) are most likely responsible for droplet growth in the shallow types (Schumacher and Houze 2003a). It should be noted that the new type 292 contains 4.13% of rain-certain pixels in 2A23 V7 for the examined two-year period. A pixel-by-pixel analysis of a three-month subset (June 1999 through August 1999) of the two-year period reveals how individual rain-certain pixels from 35°N to 35°S changed type between V6 and V7. Specifically, the analysis shows that new convective type 292 gained approximately 82% of its pixels from V6 type 152, representing a shift from stratiform to convective; overall, type 292 gained approximately 97% of its pixels from V6 stratiform rain types.

The fifth row of Fig. 7 represents anvil clouds characterized by reflectivity values of 12-16 dBZ near the surface (potentially virga) and slightly higher reflectivity values at higher levels. The 2A23 algorithm makes the distinction that a melting layer may exist for type 160 (Fig. 7m) and likely does not exist for type 170 (Fig. 7n). The reflectivity distribution aloft is similar to that of stratiform rain types; however, since rain is not evident at the surface, these types will be referred to here as anvil. Figure 8 provides an example of a TRMM PR cross section for type 160 with the vertical cross section showing echo at midlevels and no echo near the surface. Rain-certain pixels for type 300 (Fig. 7o) also exhibit this type of vertical reflectivity distribution. The anvil types may represent an evolution of forming or dissipating

stratiform rain or may simply represent thick anvil clouds that are attached to deep

convective systems (see also Schumacher and Houze 2006). Variations in height may be

linked to parent convective and stratiform regions to which the anvil is attached (Cetrone and

Houze 2011).
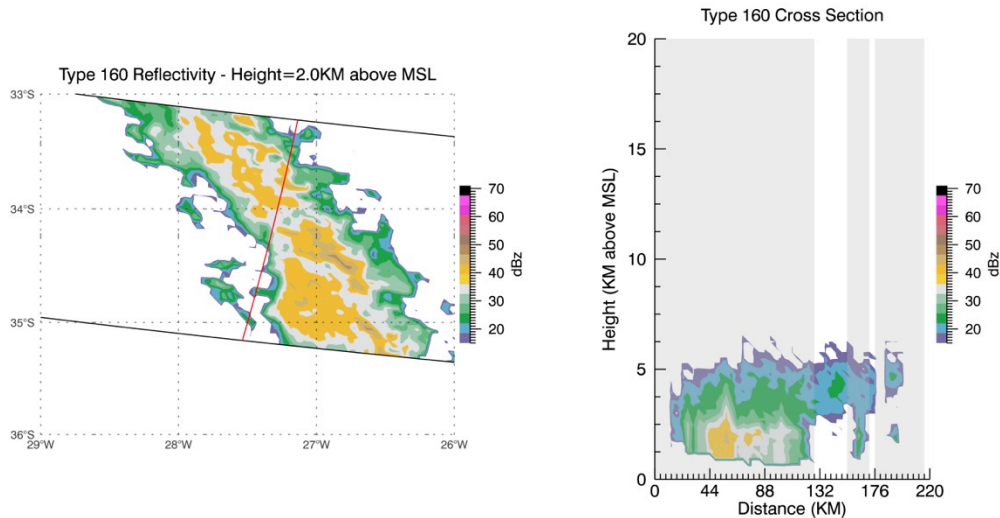
Fig. 8 – Paired horizontal and vertical cross section of TRMM PR attenuation-corrected reflectivity data for anvil type 160. Red line indicates location of vertical cross section. White areas in vertical cross section identify PR profiles classified as type 160.

Figure 9 illustrates FADs for several of the new types in 2A23 V7 and example plots

of PR reflectivity cross sections containing each type. Types 105 and 135 (Figs. 9a and 9b,

respectively) are examples of high storm height types and include data up to the 20-km level.

An analysis of a small number of cross sections for these two types indicates that their pixels

are either aged convective cells or are merely adjacent to young strong convective cells. The

final classification is stratiform owing to the detection of a bright band and/or weak

reflectivity values at lower levels, as evidenced by the FADs. Type 235 (Fig. 9c) is the only

convective high storm height type. As can be interpreted from the FAD, a portion of the data

for type 235 consists of low reflectivity values occurring at all altitudes. This is likely due to the 2A23 algorithm recognizing areas of significant noise at upper levels as rain when determining high storm height. TRMM algorithms can misidentify noise, such as ground radio interference or echo from non-meteorological targets, as real rain. The higher reflectivity values shown by the 90% quantile line on type 235 FAD begin to exhibit a shape that suggests that a portion of the data comes from real rain events. A small number of PR reflectivity cross sections for type 235 suggest that the pixels can be real rain, noise at all levels, or noise and rain that result in a false positive for high storm height (rain below, noise aloft). Both the FAD and PR cross sections suggest that the fraction of type 235 pixels having some upper level noise or cloud could be significant. However, quality control methods can be employed by the TRMM data user when identifying pixels with high storm height (Kelley et al. 2010).
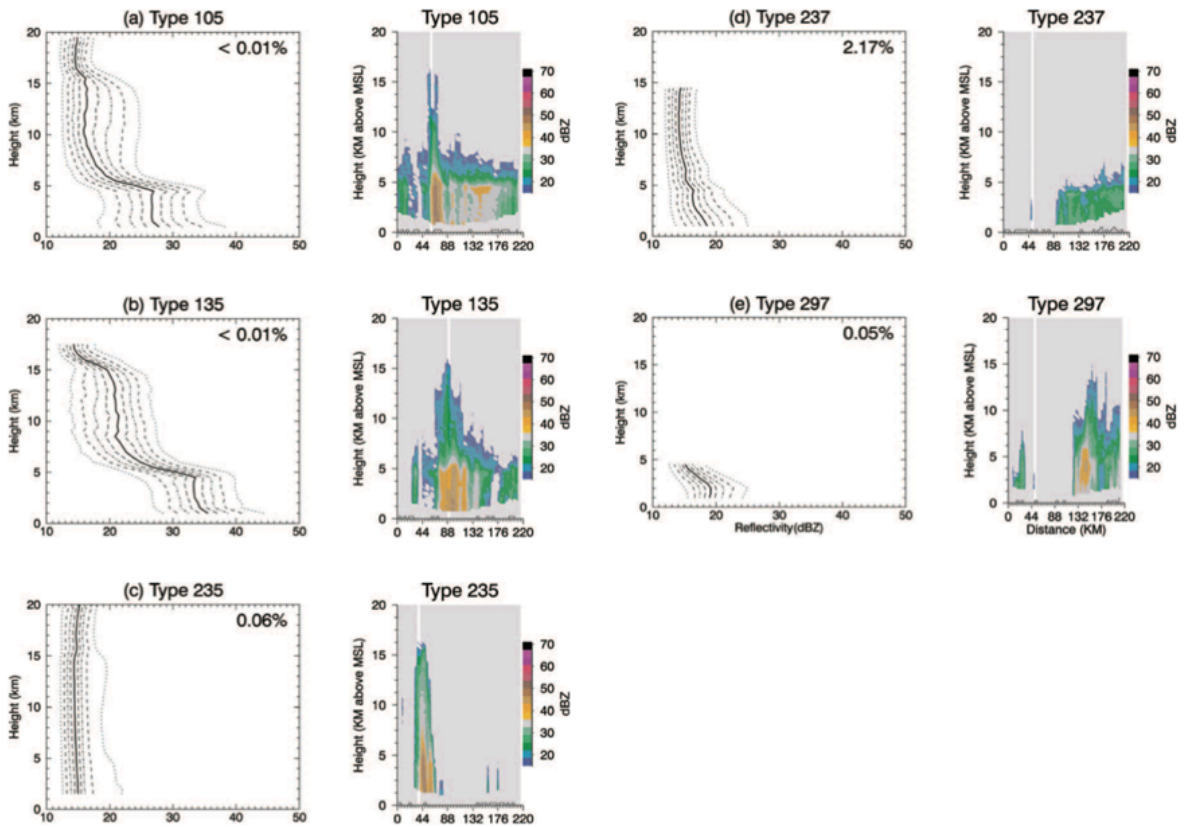
Fig. 9 - Frequency by altitude diagrams and vertical cross sections of TRMM PR 2A25-corrected reflectivity examples for new 2A23 V7 rain types. Figures 9a-c illustrate high storm height types, and Figs. 9d-e illustrate small rain cell types (June 1999-May 2000, 2008; 35°N-35°S). The percentages on the FADs represent proportions of all rain-certain pixels; the white area in the cross sections indicates the reflectivity associated with the FAD rain type. Black lines on PR cross sections indicate the level of the actual surface for each column. Cross section data are taken from orbits (a) 8684, (b) 8684, (c) 58649, (d) 58636, and (e) 8677.

Types 237 and 297 (Figs. 9d and e, respectively) are the two new small rain cell types consisting of non-shallow and shallow pixels, respectively. The type 237 FAD suggests that the echoes at levels above about 9 km are mostly noise. Again, a pixel-by-pixel analysis of V6 and V7 orbital files was performed for three months to determine how pixel types changed between the two versions. The analysis reveals that approximately 94% of type 237 pixels were previously classified as stratiform in V6. Type 297 (Fig. 9e), a small rain cell type, retains the signature characteristics of a shallow rain FAD owing to a heavy

contribution of pixels classified as type 152 in V6. Type 311 (not shown) consists of pixels that were previously classified as type 291 in 2A23 V6 but accounts for less than 0.01% of all rain-certain pixels, thus providing insufficient samples for a meaningful FAD plot.

3.3 Potential Convective Reclassifications

Progress has been made over successive versions of 2A23 to classify more shallow pixels as convective. However, it could be argued that all shallow rain, likely a product of warm-rain processes, should be treated as convective (e.g., Schumacher and Houze 2003a). Based on this argument, PR data users may consider treating two V7 stratiform rain types that contain predominantly shallow rain or rain constrained topographically (i.e., 140 and 152) as convective.

Type 140, in most regions, may be thought of as a split type in that the associated FAD (Fig. 10a) exhibits a distribution similar to an anvil cloud in the upper levels and a distribution similar to shallow rain types in the lower levels, with weak reflectivity values in between. However, there are specific regions where type 140 reflectivity distributions do not share this shape. For instance, over the Tibetan Plateau, the FAD indicates elevated convection (Fig. 10b) where type 140 occurrences peak during the warmer seasons (Fig. 11). Rain at the eastern edge of the Tibetan Plateau during the warm spring season is mostly convective (Li et al. 2010). In the summer months, the peak concentrations for type 140 shift west and spread to the central Tibetan Plateau (Fig. 11c).
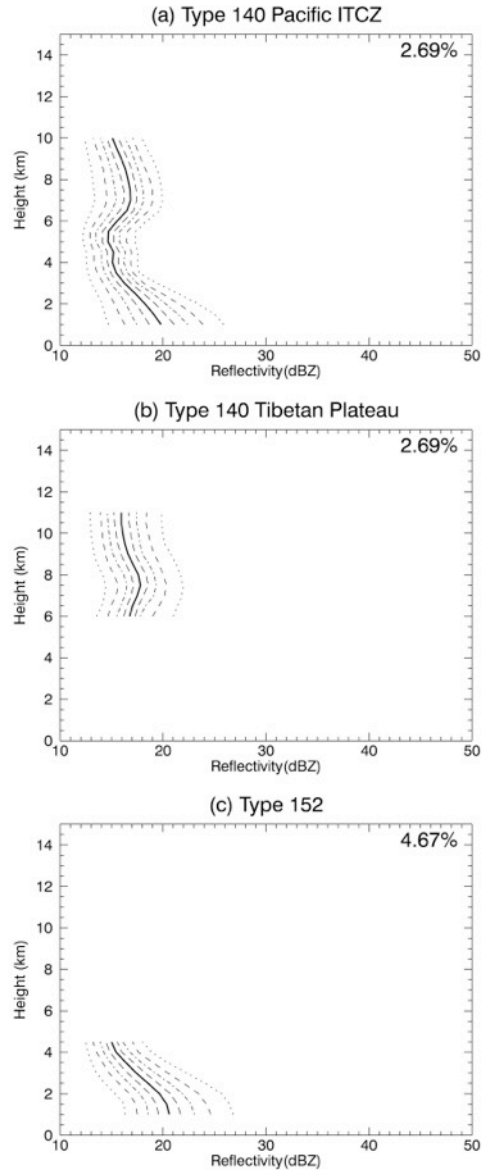
Fig. 10 - Frequency by altitude diagrams of TRMM PR 2A25-corrected reflectivity (June 1999-May 2000, 2008) showing (a) type 140 over the Pacific ITCZ (69°N, 1155-180°W), (b) type 140 over the Tibetan Plateau (30-35°N, 80-95°E), and (c) type 152 (35°N-35°S, 180°E-180°W). The percentages represent proportions of all rain-certain pixels.
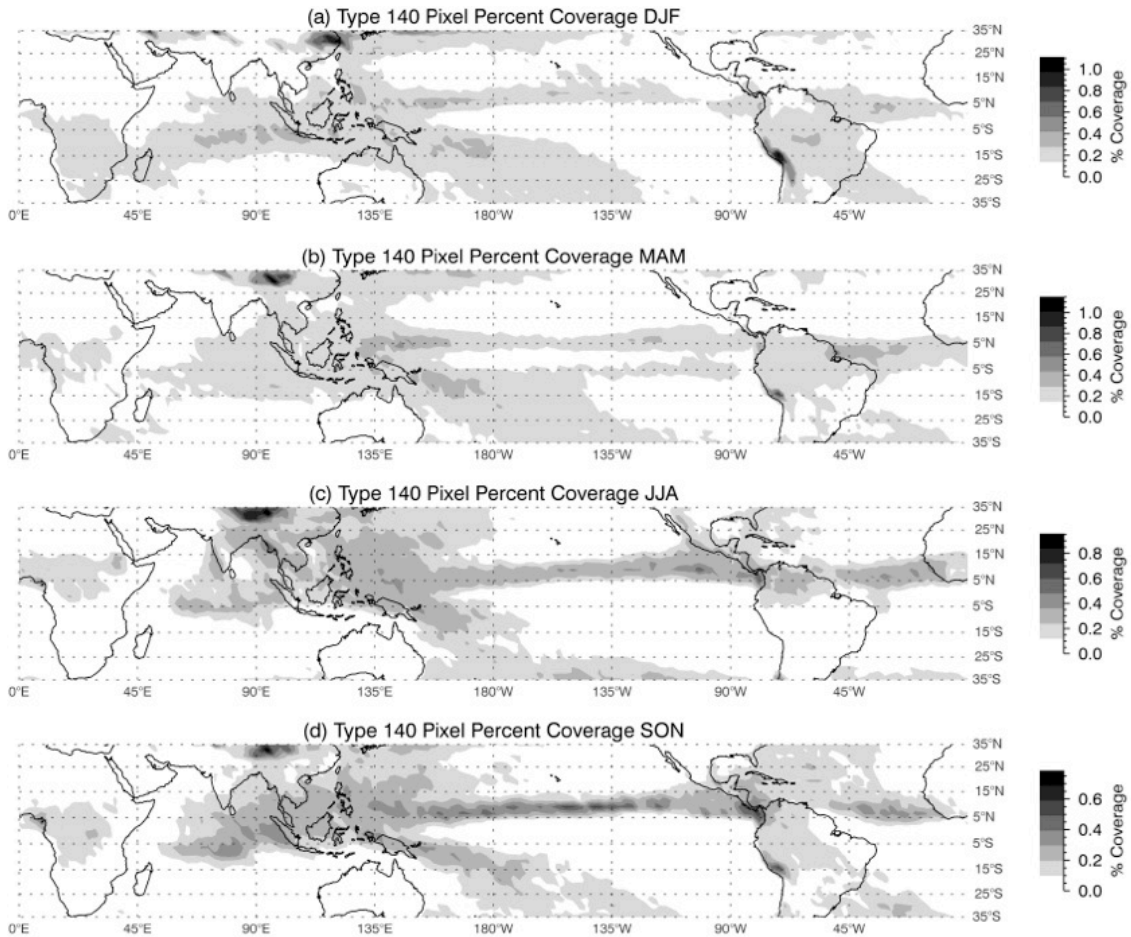
Fig. 11 - Seasonal percent coverage maps showing the occurrence of TRMM PR pixels for type 140 (June 1999-May 2000, 2008) during months (a) DJF, (b) MAM, (c) JJA, and (d) SON.

During this time, moisture increases in the boundary layer, making it conditionally unstable to moist convection (Fujinami and Yasunari 2001). Fu and Liu (2007) found that much convective activity over the Tibetan Plateau was likely misclassified as stratiform by the V5 and V6 PR algorithms. The introduction of new convective rain types such as type 237 has likely resolved some of the misclassifications in this region. Approximately 94% of type 237 pixels came from 2A23 V6 stratiform rain types during the examined three-month period, likely impacting the Tibetan Plateau region. Cross sections of PR reflectivity during

28

summer in the Tibetan Plateau (Fig. 12a) indicate that type 140 rain in this region is mountain convection. In areas over the tropical ocean, type 140 appears as either shallow rain near the surface, anvil cloud aloft, or sometimes both (Figs. 12b and 12c). At these tropical latitudes, type 140 rain is likely generated by warm-rain processes; thus, such rain can be considered convective.

Type 152 consists of pixels classified as shallow non-isolated by 2A23 and is the only shallow stratiform type (see Table 1). Pixels are identified as shallow by 2A23 when the storm top height is at least 1 km below the 0°C level, and confidence is high when the storm top height is 1.5 km below the 0°C level. By comparing the 152 FAD in Fig. 10c with the shallow isolated and shallow non-isolated convective types in Figs. 7g-7l, the similarities are clear. Furthermore, cross sections of PR reflectivity (Fig. 12d) illustrate that type 152 pixels appear as shallow convective rain cells or appear adjacent to shallow convective rain. Additionally, in an effort to accurately classify additional shallow non-isolated pixels as convective in 2A23 V7, the concept of "randomly" appearing shallow non-isolated pixels was created, resulting in new convective rain types. As noted in section 3.2, type 152 V6 contributed to approximately 82% of type 292's pixels for the three-month comparison. Given this trend of pixel movement out of type 152 to shallow convective rain types, and the fact that type 152 pixels are already a shallow rain type (and thus likely produced by warm-rain processes), type 152 V7 pixels could be treated as convective rain.
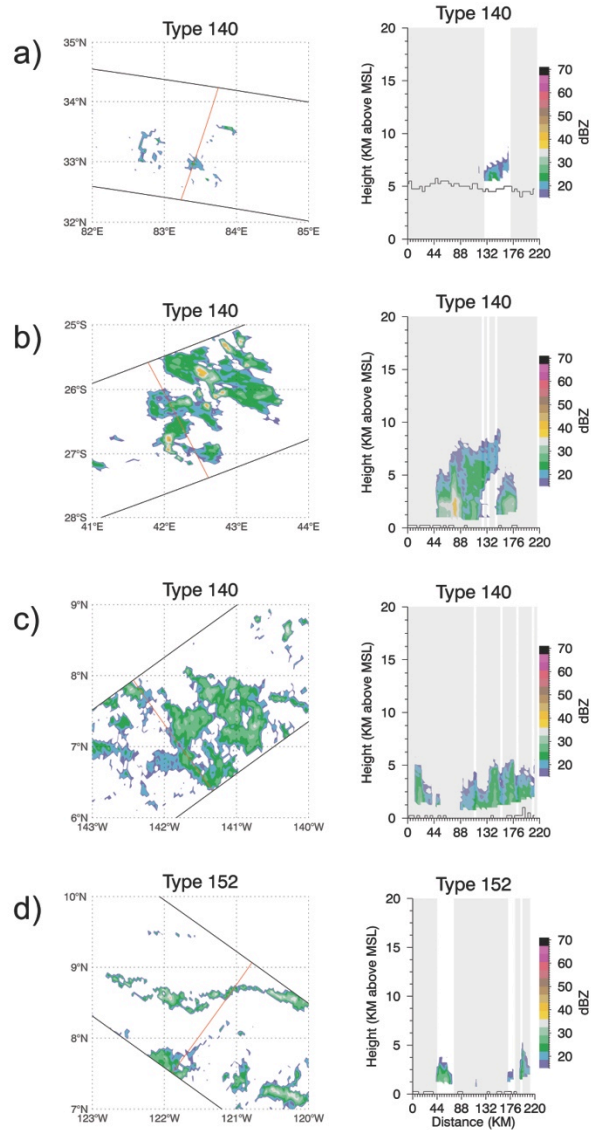
Fig. 12 - TRMM PR retrieval swaths (left column) and vertical cross sections (right column) using 2A25-corrected reflectivity. Red line in swath indicates the location of the vertical cross section. The white columns in the vertical cross sections highlight pixels of (a) type 140 convection over the Tibetan Plateau, (b) type 140 anvil over the Indian Ocean, (c) type 140 shallow convection over the Pacific Ocean, and (d) type 152 over the Pacific Ocean. Black lines on vertical cross sections indicate the level of the actual surface for each column. PR swath data height/orbit: (a) 6 km/8677, (b) 4.5 km/8796, (c) 2 km/10149, and (d) 2 km/9784.

30

We have presented evidence that types 140 and 152 generally show convective characteristics and could be treated as convective, but it is possible that some pixels could be erroneously reclassified from stratiform to convective when implementing these reclassifications. For instance, the 2A23 algorithm classifies instantaneous rain data. Shige et al. (2004) argued that rain is not the result of the latent heating that occurs during a rain event but of the accumulated latent heating generated for a finite period prior to a rain event. By this measure, it is possible that some shallow rain, for example, may not be entirely attributable to warm-rain processes alone. The decision of whether to follow these suggestions is left to the reader, who may wish to consider restricting reclassifications to certain geographical locations or times of year.

3.4 V7 Stratiform Rain Fraction and Reclassification Results

Schumacher and Houze (2003b) used V5 TRMM PR data to determine the geographical distribution of the stratiform rain fraction across the tropics (Fig. 13a); they found that the tropics-wide average was 40%. An updated analysis of the tropics-wide (20°N-20°S) stratiform rain fraction was performed following the methods used by Schumacher and Houze (2003b) for comparison. The comparison with V5 is warranted given the trend over several algorithm updates to classify more PR profiles as convective, especially in the shallow categories, and the wide usage of statistics from the Schumacher and Houze (2003b) study. For rain calculations, near-surface reflectivity values from 2A25 were separated into 2-dB bins for stratiform and convective rain types. Only average reflectivity values of greater than or equal to 17 dBZ (i.e., the 16-18 dBZ histogram bin) were considered. Note that Schumacher and Houze (2003b) used 1-dB bins but results should

still be comparable between the two studies. The V5 initial reflectivity-rainrate (Z-R) relationships for convective ($Z = 148R^{1.55}$) and stratiform ($Z = 276R^{1.49}$) rain (Iguchi et al. 2000) were then used to calculate rain rates for the examined two-year period.
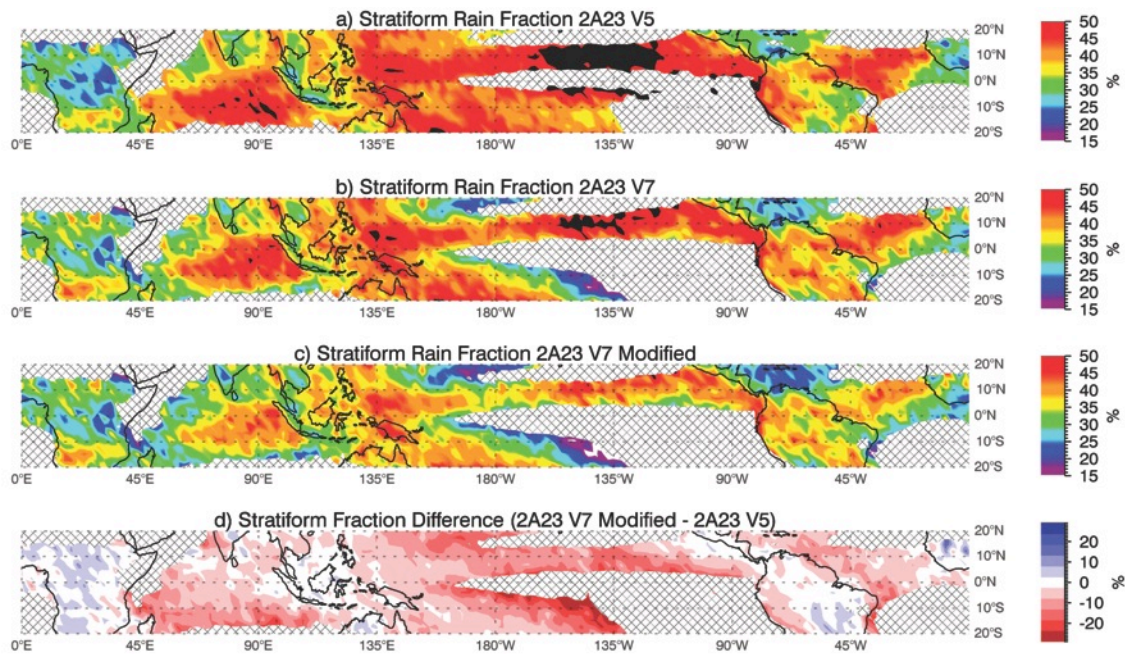
Fig. 13 - TRMM PR stratiform rain fractions calculated using 2A25 near-surface reflectivity values gridded to 2.5° with (a) Fig. 3d from Schumacher and Houze (2003b) showing V5 data with a modified color bar, (b) 2A23 V7 standard rain-type classifications, (c) 2A23 V7-modified classifications with types 140 and 152 as convective, and (d) the difference between Fig. 13c and Fig. 13a. Data for (a) from 1998 to 2000. Data for (b) and (c) are from June 1999 to May 2000 and 2008. Fractions greater than 50% are black. Crosshatched areas indicate average yearly rain less than 0.6 m yr^{-1} and were excluded.

The resulting V7 tropics-wide stratiform rain fractions are illustrated in Figs. 13b and 13c. Figure 13b uses the standard 2A23 V7 stratiform and convective classifications and the V5 initial stratiform and convective Z-R relationships to provide an overall stratiform rain fraction of approximately 38%. Figure 13c employs the suggested reclassifications of section

3.3, resulting in an overall stratiform rain fraction of approximately 35%. Figure 13d

illustrates the difference in the stratiform rain fraction between the results of Schumacher and

Houze (Fig. 13a) and the results from the modified 2A23 classifications (Fig. 13c). While the

overall stratiform rain fraction decreases by 5%, higher regional variability is evident with

the stratiform rain fraction increasing over land areas, with some exceptions, and decreasing

over the oceans, with the largest decreases seen over the Pacific Ocean.

Initial PR Z-R relationships used were from V5 so that results could be compared

directly with those of Schumacher and Houze (2003b). However, the initial Z-R relationships

for V7, proposed by Iguchi et al. (2009), are different for stratiform ($Z = 256R^{1.50}$) and

convective ($Z = 151R^{1.58}$) rain. The same stratiform rain fraction calculations using these Z-R

relationships result in tropical stratiform rain fractions of nearly 41% when using standard

2A23 V7 rain-type classifications and decrease to approximately 37% when using the rain-

type reclassifications suggested in section 3.3. The increase in the stratiform rain fraction

obtained using the initial V7 Z-R relationships compared to the previous results using the

initial V5 Z-R relationships (i.e., 38% and 35%) seems counterintuitive, given the observed

net reduction in stratiform pixels (see Table 1) between 2A23 V6 and V7 for the examined

two-year period. It should also be noted that the 2A25 algorithm modifies the initial Z-R

relationship for most pixels, such that stratiform rain fractions calculated from the 2A25 rain

rate (rather than reflectivity) variables may be different than the results presented in Fig. 13.

The change in near-surface bin height between 2A25 V6 and V7 may also play a role

in the change in the stratiform rain fraction. For near-surface data, the lowest noise-free bin is

selected as the near-surface bin; thus, the bin number, and therefore, the height of a near-

surface pixel can vary on a per-pixel basis. A direct comparison between 2A25 V6 and V7

33

data will show that, on average, the height of the near-surface bin has increased owing to differences between the two versions. For instance, the tropics-wide (20°N-20°S) height of the near-surface bin for June 1999 has increased from ~1.05 km to ~1.28 km between V6 and V7. An inference made on the basis of FADs from Fig. 7 suggests that increasing the near-surface bin height from ~1 km for deep convective types (Figs. 7d-f) might lower reflectivity and total convective rain. Furthermore, Fig. 7a suggests that stratiform reflectivity and rain may not decrease as much as the deep convective types with an increase in the near-surface bin height from ~1 km. If this were true, it would act to increase the stratiform rain fraction to some degree; however, this analysis suggests that factors such as the movement of shallow pixels from stratiform to convective types have acted, on the whole, to decrease the tropics-wide stratiform rain fraction.

3.5 Shallow Non-isolated Rain

Figure 14 illustrates echo coverage maps for the major categories based on 2A23 V7 classifications: stratiform, convective, shallow isolated, shallow non- isolated, and anvil. The shallow isolated and shallow non-isolated categories consist of the types listed as such in Table 1. The anvil category consists of types 160, 170, and 300. The stratiform and convective categories consist of types 1xx and 2xx that are not included in the categorizations above (i.e., no shallow isolated, shallow non-isolated, or anvil). Stratiform and convective pixels exhibit a similar geographical distribution, while shallow isolated pixel occurrences show a unique geographical distribution with maxima in the southern Indian and Pacific oceans (Schumacher and Houze 2003a). Anvil pixels are collocated with regions of deep convection (Schumacher and Houze 2006, Li and Schumacher 2011). Shallow non-

34

isolated pixels occur most commonly over the Pacific intertropical convergence zone (ITCZ). While there are very few shallow non-isolated pixels over land (similar to the shallow isolated category), a notable amount occurs over South Asia, the Maritime Continent, and the Amazon. Overall, shallow non-isolated pixels occur in regions where convective, stratiform, and anvil pixels maximize; thus, they are more likely associated with deep convective systems than their isolated counterparts.
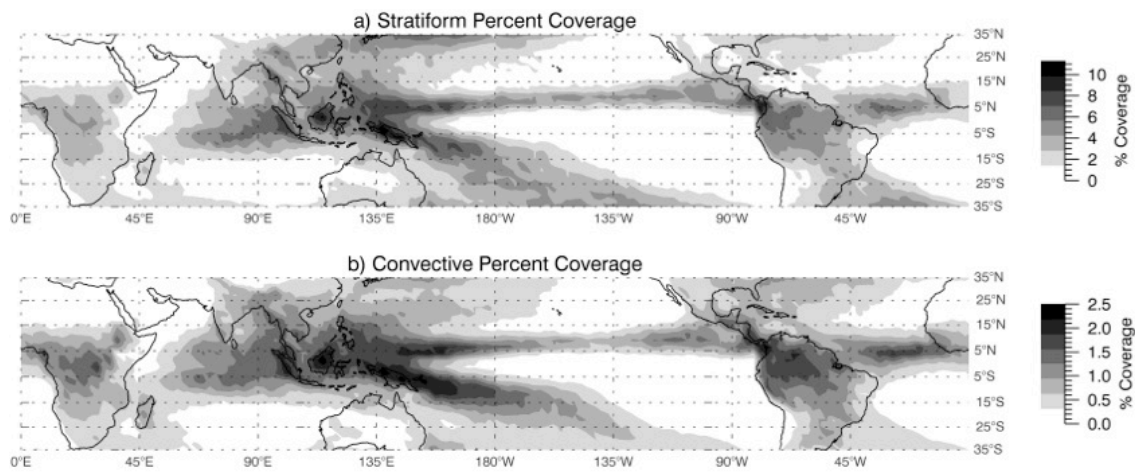
Fig. 14 - Percent coverage maps showing the occurrence of TRMM PR pixels for June 1999 through May 2000 and all of 2008 showing (a) stratiform pixels excluding types 152, 160, and 170, (b) convective pixels excluding shallow types, (c) shallow isolated types, (d) shallow non-isolated types, and (e) anvil types 160, 170, and 300. Further details are provided in Table 1.
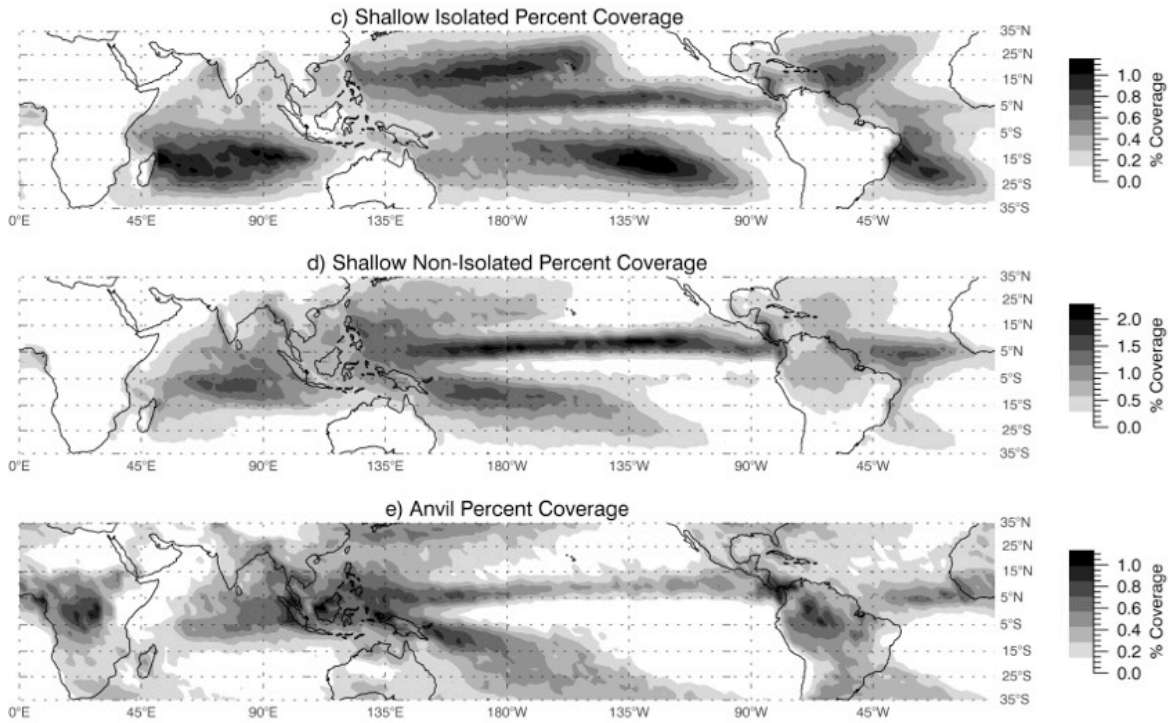
Fig. 14 - Continued

Figure 15 illustrates percentages of total rain for shallow isolated and shallow non-isolated rain types during the examined two-year period. Shallow isolated rain accounts for the majority of rain in areas with cold sea surface temperatures in the southeast Pacific and south Atlantic and for a significant amount of rain in the trade wind regions. Shallow non-isolated rain also contributes to a significant amount of rain in the trade wind regions (i.e., just outside the oceanic ITCZ bands) and contributes to total rain over tropical land areas, where shallow isolated pixels do not.
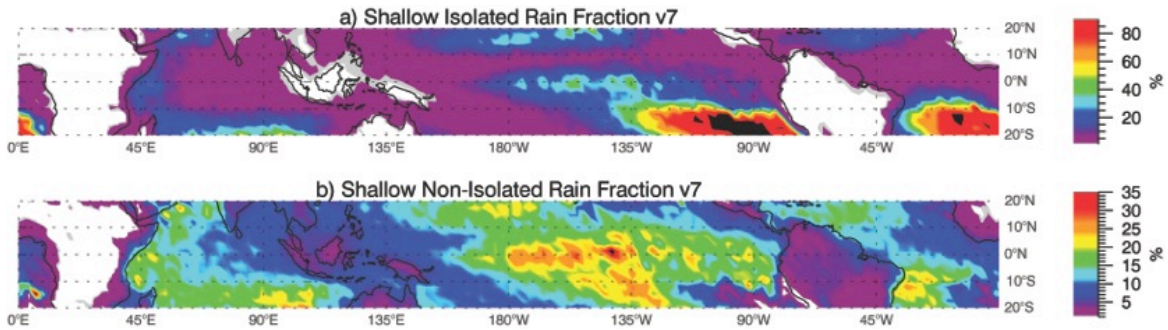
Fig. 15 - TRMM PR shallow rain fractions calculated using 2A25 V7 near-surface reflectivity values gridded to 2.5°(June 1999-May 2000, 2008) for (a) shallow isolated where areas greater than 90% are black and (b) shallow non-isolated rain where areas greater than 35% are black. Areas less than 1% are white for (a) and (b).

Shallow non-isolated rain was a concept introduced in 2A23 V6 to represent shallow rain pixels that are not isolated from non-shallow rain pixels. In section 3.2, it was noted that type 152 contributed to approximately 82% of type 292 pixels in V7 for the examined three-month period. This is likely due to the introduction of the concept of "randomly" occurring pixels. It is clear that more effort has been made to identify the convective pixels in the stratiform rain types in V7, and this has resulted in pixels moving out of type 152 between V6 and V7. This leaves shallow pixels in type 152 yet still classified as stratiform by 2A23. An analysis of a small number of PR cross sections for type 152 indicates that these pixels occur in a number of scenarios, including in areas of rain between convective cells and along edges of isolated convective rain cells (Fig. 16). The relatively high occurrence of types 152 and 292 in the Pacific ITCZ warrants future study.
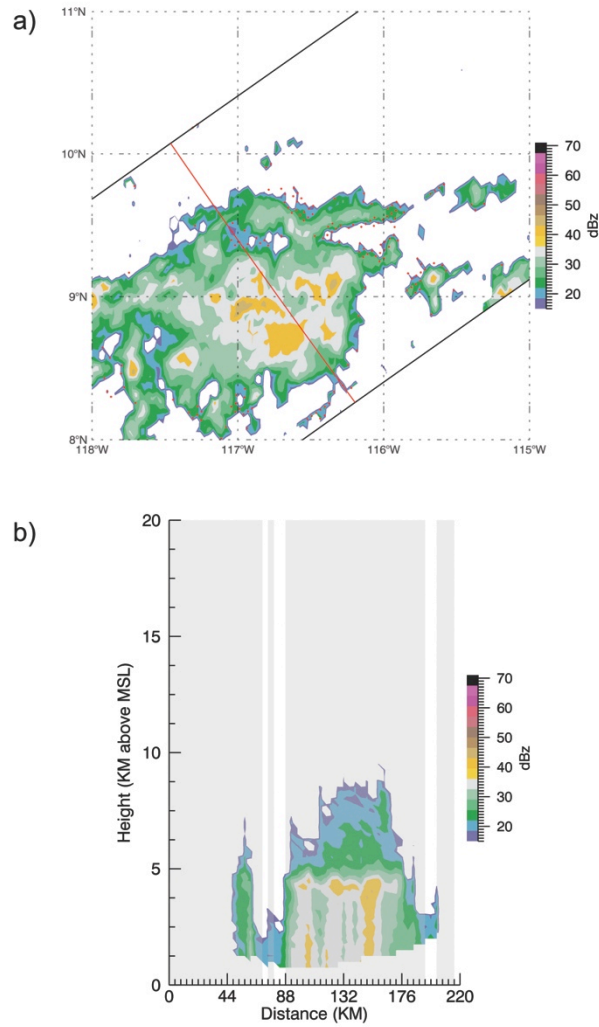
Fig. 16 - TRMM PR retrieval (a) swath and (b) vertical cross sections of 2A25-corrected reflectivity highlighting locations of type 152 pixels relative to larger areas of rain in the Pacific ITCZ. Type 152 pixels are highlighted by red dots in (a) and white channels in (b). Red line in (a) indicates the location of the vertical cross section (b). PR swath data are plotted at 2 km above the mean sea level for orbit 61514. Black lines on the vertical cross section indicate the level of the actual surface for each column.

4. PR ALGORITHM 2A25 AND DISDROMETER MEASUREMENTS

The TRMM 2A23 rain types are a major input into the TRMM 2A25 algorithm, which has the primary task of correcting PR-observed reflectivity profiles for attenuation and estimating rain rate from the corrected radar reflectivity. The performance of TRMM PR rain rate estimates made by 2A25 can be evaluated by comparing near-surface PR data to rainfall data collected at the ground. Accurate global rain estimates have wide-ranging implications from determining the impacts of hurricanes and flash floods to assessing changes in the hydrological cycle over long time scales.

Surface rainfall estimates by the PR over land and ocean in the tropics have evolved with advancing algorithm versions (e.g., Islam and Uyeda 2007, Seto et al. 2011, Kirstetter et al. 2013). For example, Schumacher and Houze (2006) showed that convective rain rates were higher over West Africa and lower over the adjacent East Atlantic using V5 data, whereas and Futyan and Del Genio (2007) showed the opposite using V6 data. A significant body of literature on the intensity of convective systems over West Africa suggests that V6 went the wrong direction. A recent study using ground radar has shown that 2A25 V7 products over the southern conterminous United States (CONUS) have improved on overestimation biases at low rain rates and underestimation biases at high rain rates compared to V6, but still underestimate rain overall (Kirstetter et al. 2013). However, this study did not address the reasons why the 2A25 algorithm may be underperforming. Underestimation of intense rainfall over South America in V7 also seems to be occurring (Rasmussen et al. 2013).

Since the launch of TRMM, NASA has conducted a ground validation campaign in order to evaluate the satellite's observations since its launch. Validation sites operated by

NASA include the Kwajalein Atoll in the Republic of the Marshall Islands; Melbourne, Florida; Houston, Texas; and Darwin, Australia (Wolff et al. 2005). The instrumentation at each site varies, but includes tipping bucket rain gauges to measure rain accumulation. Additionally, Texas A&M University has maintained two instrument sites in southeast Texas (College Station and Alvin). The instrumentation at each site consists of a single Joss-Waldvogel impact disdrometer, which measures the drop size distribution (DSD) of rain hydrometeors, and two co-located tipping bucket rain gauges. The two sites have yielded multiple years of disdrometer and rain gauge data, although not continuously.

In order to determine if the 2A25 algorithm products contain biases in the PR rainfall data over land and why these biases may still persist, comparisons to ground-based observations from rain gauges, disdrometers, and radars can be made. This study uses long-term disdrometer measurements from Southeast Texas, which provide direct information about the raindrop size distribution from which rainfall parameters such as radar reflectivity factor and rain rate can be derived, to assess V6 and V7 retrievals from the PR 2A25 algorithm.

4.1 Disdrometers

Historically, DSDs were determined by measuring the size of raindrops that fell on filter paper (e.g., Marshall and Palmer 1948). Joss and Waldvogel (1967) invented an impact disdrometer, which measures the impact energy of a raindrop and assumes a fixed relationship between drop diameter and terminal velocity to record the size of rain drops into one of 20 bins. From these measured DSDs, several rainfall parameters can be calculated such as radar reflectivity factor (Eq. 1) and rain rate (Eq. 2)

$$[1] \quad\quad\quad\quad Z = \int_0^\infty N(D)D^6\,dD$$

$$[2] \quad\quad\quad\quad R = \frac{6\pi}{10^4} 6\pi \int_0^\infty N(D)D^3 v(D)\,dD$$

where D is the drop diameter and v(D) is equal to the terminal fall velocity of a drop.

Following the development of methods for measuring DSDs, it was found that the relationship between reflectivity and rain rate is not a fixed one, but instead varies from region to region. Battan (1973) published a list of more than 60 Z-R relationships from all over the world with values of the parameter a varying from 24.7 to 865. For reference, the Z-R relation used by the national weather service for NEXRAD rain rate estimation is $Z=300R^{1.4}$. Accurate Z-R relations are important for accurate rainfall estimates from radar, especially in areas where other ground-based rainfall measurements are sparse or not available. The DSD data collected using disdrometers can be used to determine a regional Z-R relationship. However, several issues must be considered when determining a Z-R relation using DSD data.

Smith et al. (1993) highlighted issues with the accuracy of rainfall parameters calculated using drop samples from a known population. Simulations were designed and run by Smith et al. that generated DSD samples with fixed drop counts. Rainfall parameters were calculated from the simulated DSD samples and compared to the true rainfall parameter values calculated from the entire drop population, which were known. The findings show that the median value of DSD-derived radar reflectivity estimates is within 3 dB of the known population radar reflectivity value when the drop count for a DSD sample is 100 drops. This value falls to 7 dB for DSD samples with drop counts of 20. For rain rates, the median value

of rain rate estimates is within 1 dB of the known population value when the drop count for a DSD sample is 100. Therefore, the accuracy of rainfall parameters estimated from DSD samples is increased when the sample size increases.

The design of the impact disdrometer itself has limitations. For instance, impact disdrometers are sensitive to noise and this can affect sensitivity to smaller drops. Tokay et al. (2003) note that during testing, background noise of 70 dB almost completely suppressed the detection of drops from 0.3 to 0.8 mm in diameter. The hardware is created with a thresholding capability that allows for the rejection of drops when noise level is high. However, as noise levels increase during events with large raindrops owing to the drops themselves, smaller drops are rejected as noise. This is known as the dead time issue (Tokay and Short 1996). Therefore, caution should be taken when considering J-W disdrometer measurements of drops less 1.0 mm in diameter. However, these size drops don't normally contribute substantially to overall rain accumulations.

Joss-Waldvogel (JW) impact disdrometers along with co-located tipping bucket rain gauges were deployed at two ground sites in southeast Texas where they collected regional rainfall statistics from 2004 to 2013. These sites were located in College Station (30.646N, -96.298W) and Alvin (29.440N, -95.273W), Texas (Figure 17).
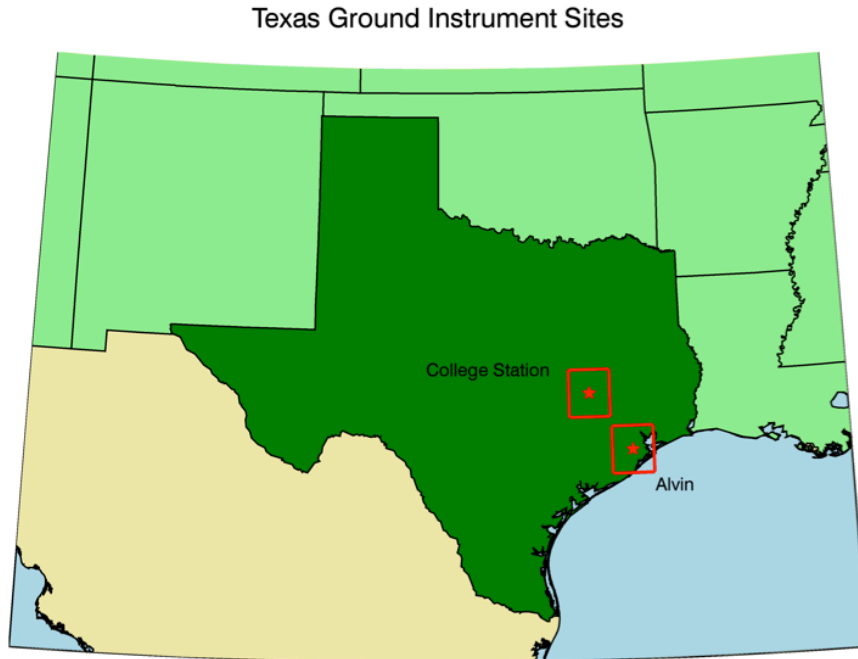
Fig. 17 - Location of College Station and Alvin instrument sites in southeast Texas. Stars indicate location of site while 1°x1° boxes show domain for which TRMM 2A25 data was selected for comparison to disdrometer data.

DSD samples collected by an impact disdrometer are typically collected with a fixed sampling time. DSD samples at the College Station and Alvin sites were collected as either 10-second or 1-minute samples. DSD samples can be combined or averaged over time to increase drop count, but this might also have the effect of masking some of the variability apparent with shorter sample times. Figure 18 demonstrates the effect of time averaging showing that that as the length of the sampling time for a DSD sample increases from 1 min to 10 min, smaller values of radar reflectivity and rain rate occur less frequently and higher values of R are associated with the same Z. When preparing a DSD dataset for use in the calculation of a Z-R relationship, a balance must be struck between time averaging practices and DSD sample drop counts so that the drop counts are high enough to provide more accurate rainfall parameters yet the samples are not averaged so much that too much

43

microphysical variability is removed from the data set. DSD are hereafter averaged in 1-min samples because that is the community standard; however, it could be argued that longer samples are warranted because of the relatively large footprint of the TRMM PR (i.e., 5 km diameter at nadir) and thus the larger sample volume.
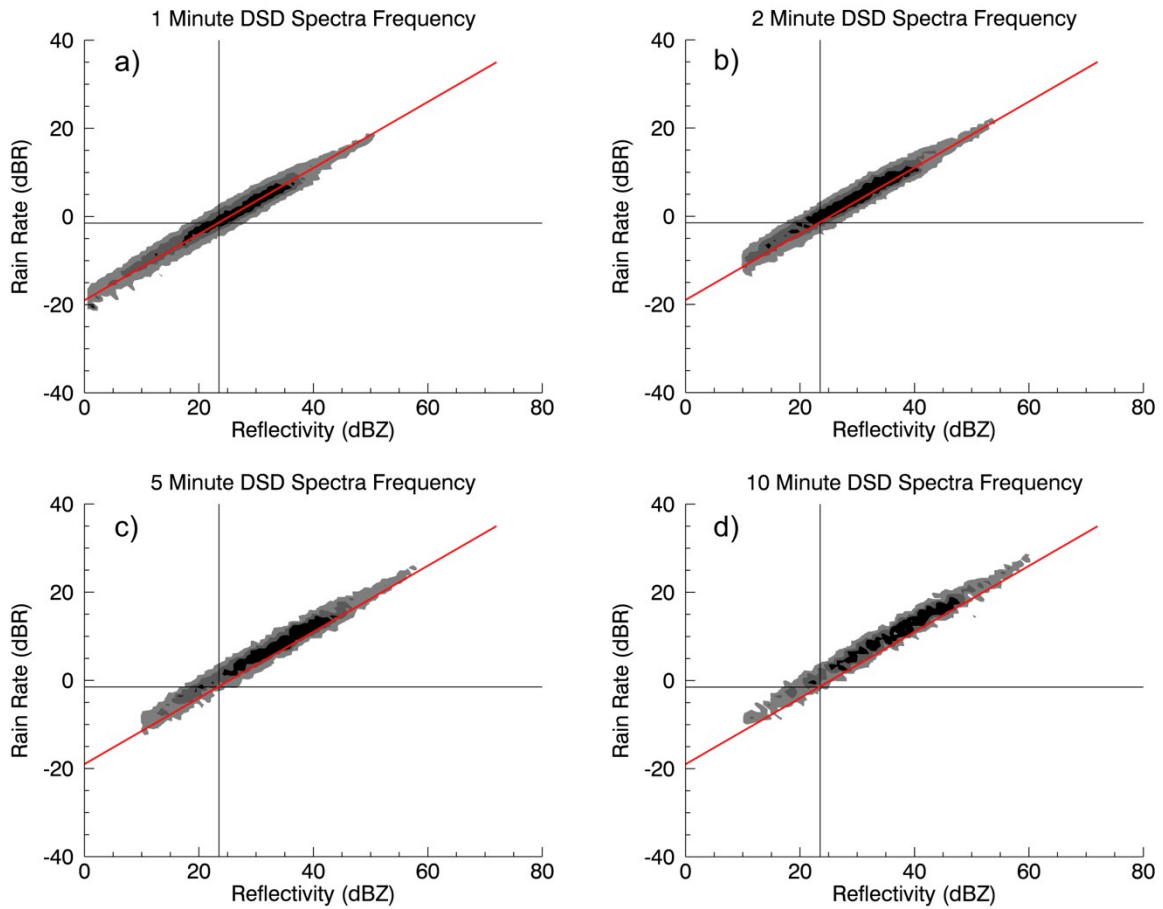
Fig. 18 - DSD time averaging contour plots for rainfall parameters radar reflectivity factor and rain rate. Contours show a normalized frequency of occurrence for the rainfall parameters for (a) 1-min, (b) 2-min, (c) 5-min and (d) 10-min time averaged DSD spectra using the same DSD source data.

4.2 Disdrometer Methods and Results

Storms were identified in the DSD data for each site utilizing previously established methodology, rainfall parameters were calculated for the storm DSD samples, and a climatological Z-R relationship was calculated based on the DSD-derived rainfall parameters. Rainfall parameters from the disdrometer data are then compared to TRMM 2A25 near-surface reflectivity data from southeast Texas. TRMM over flights of the College Station and Alvin instrument sites within +/- 3 hours of the start and end times of each storm were identified. All stratiform and convective PR rain retrievals within the 1°x1° domain centered on each site (see Fig. 17) were used for the comparison.

The processing of DSD data from both sites proceeded by identifying rain events in the data. Using the criteria established by Steiner and Smith (2000), rain rates were calculated for 1-min DSD samples and those with rain rates equal to or exceeding 0.1 mm/hr were identified. These DSD samples were grouped and then split into separate events when separated by at least 6 hours a la Steiner and Smith. An event with rain accumulation of 2.5 mm or more was identified as a rain event or storm. From October of 2007 through June of 2011, 105 storms were identified in the Alvin data while 315 storms were identified in the College Station data from October of 2004 through March of 2013. Once the storms were identified, radar reflectivity and rain rates were calculated for each 1-min DSD sample and a linear regression was performed by finding a least squares fit solution to the equation

[3] $\qquad y = \log(a) + b*x$

45

where y = logR and x = logZ. The solution of regressing R on Z, as was done in this case, is not the same solution found when regressing Z on R. Steiner and Smith (2000) noted that in estimating rain rates from radar reflectivity, Z is the independent variable so a power law of $R=aZ^b$ was found and converted to the more conventional form of $Z=aR^b$.

Figure 19 shows all the 1-min DSD samples for both sites as well as the calculated climatological Z-R relationship ($Z=177.3R^{1.66}$). Separate calculations were done for each site (not shown), but there was no apparent difference between the DSD parameters between Alvin and College Station so data from the two sites are hereafter combined to improve sampling.
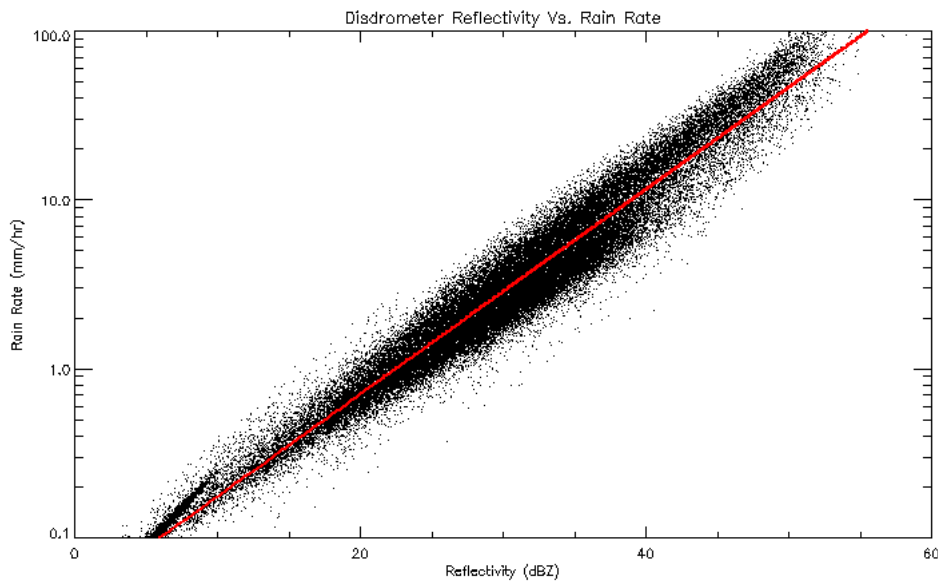

Fig. 19 – DSD-derived rainfall parameters of radar reflectivity and rain rate pairs for DSD samples with drop counts >= 100 and rain rates >= 0.1 mm/hr from both College Station and Alvin instrument sites. The red line indicates the climatological Z-R curve of $Z=177.3*R^{1.66}$.

4.2.1 Disdrometer Comparison to TRMM PR

Figure 20 shows the population of TRMM PR Z-R pairs that are coincident with the disdrometer-defined rain events. The PR clearly separates convective (red points) and stratiform (blue points) rainfall in Z-R space, with convective rain generally assigned a higher rain rate than stratiform rain at the same reflectivity. However, the Z-R point population becomes more scattered above 30-35 dBZ, with some intermingling of convective and stratiform points (esp. in V7).

Algorithm changes between V6 and V7 (Iguchi et al. 2009) include a change to the DSD model (i.e., initial Z-R relationships for convective and stratiform rain) and the reintroduction of non-uniform beam filling (NUBF) after it was removed from V6 entirely. An error found in the V5 NUBF methods was fixed for V7 and has the greatest impact of increasing reflectivity and rain rates in highly convective situations (Kirstetter et al. 2013). At low reflectivities, V7 rain rate retrievals vary more from the initial Z-R relation compared to V6 (i.e., they do not fall as much along a hard line). At higher reflectivities, V7 rain rate retrievals appear to have less spread compared to V6 and include two hard stops offset from the initial Z-R relation lines. The reason for these hard stops will be addressed later in the section.

When compared to the climatological Z-R relation calculated using the DSD data from the two instrument sites (solid line in Fig. 19), the V7 convective data appear to be an improvement over the V6 data as the V7 Z-R points more closely follow the climatological Z-R relation. However, the stratiform data in V7 appear to be further away from the climatological Z-R line, giving lower rain rate values for the same Z compared to V6.
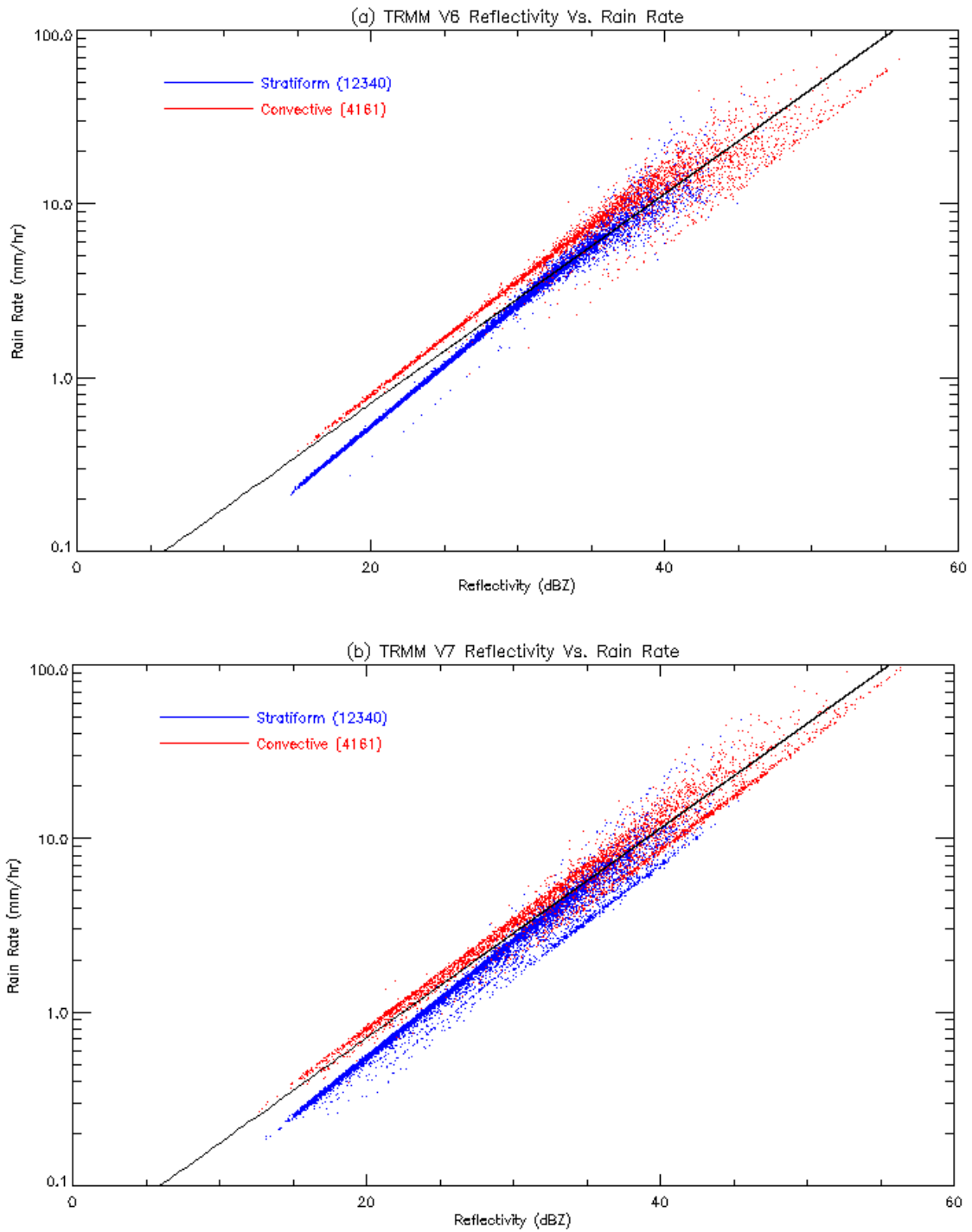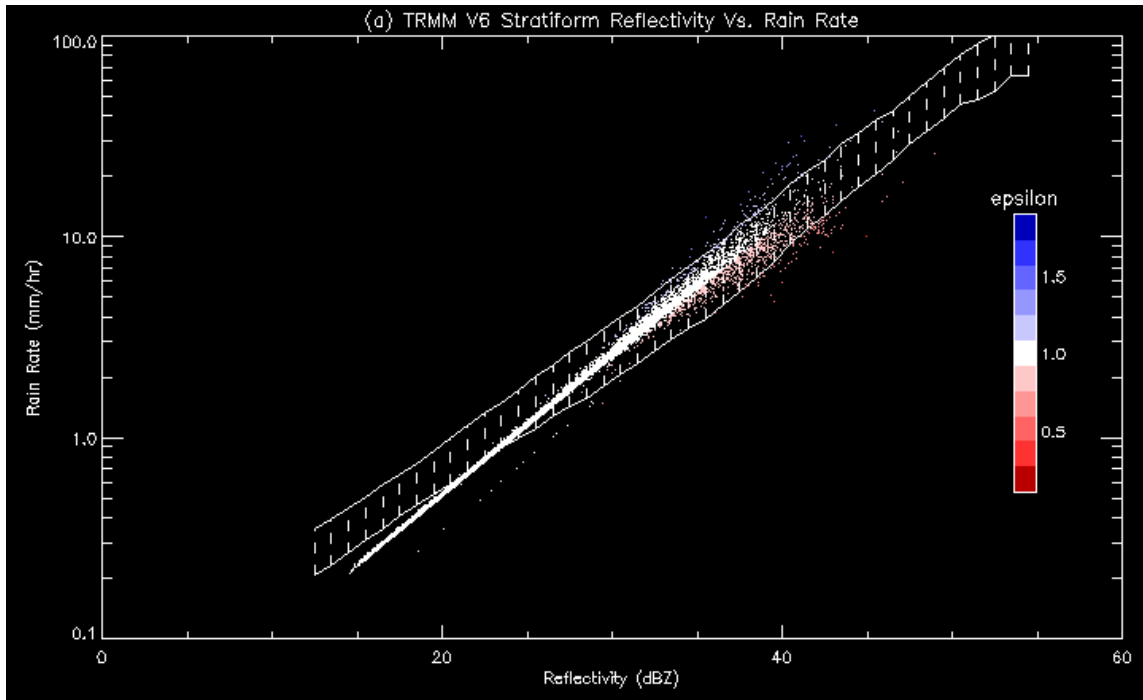
Fig. 20 – Attenuation corrected near-surface reflectivity and rain rate data from TRMM 2A25 (a) V6 and (b) V7 algorithm for College Station and Alvin Texas. TRMM data is coincident with occurrence of storms identified in DSD data. Black line indicates climatological Z-R relationship identified in red in Fig. 19.

An interesting question to ask at this point is if the scatter evident in the V6 and V7 PR retrievals seen in Fig. 20 is consistent with the scatter in the disdrometer-based climatology in Fig. 19. To address this question, Figs. 21 and 22 show the standard deviation of the disdrometer population compared to the PR stratiform and convective Z-R points, respectively. Figures 21 and 22 also color-code the Z-R points for values of epsilon in order to understand the possible cause of PR points that fall outside of the disdrometer standard deviation values and of the hard stops in V7.

While the majority of TRMM PR stratiform points in Fig. 21 fall within the spread of the disdrometer data, notable exceptions occur where the PR points are below the disdrometer spread (i.e., the PR assigns lower rain rates at the same reflectivity compared to the disdrometer climatology). This is especially the case at $Z < 20$ dBZ, where epsilon is equal to 1 in all cases, and $Z > 30$ where epsilon values are $\ll 1$. When epsilon is $\gg 1$, the PR points are above the disdrometer spread. Because the sensitivity of the disdrometer and PR suffer at small drop sizes and low rain rates, the remaining focus will be on comparisons at higher reflectivities and rain rates. It is apparent that epsilon is playing an important role in determining stratiform rain rates at higher reflectivities and that extreme epsilon values put the PR Z-R points outside of the disdrometer climatology. In most cases, extreme epsilon makes the stratiform rain rates weaker than what the ground instrument would assign, which may significantly impact rain rate distributions and overall rain accumulations. While both V6 and V7 show similar sensitivity to epsilon variations, V7 shows more spread in Z-R points and a greater underestimation of stratiform rain. V7 also shows more extreme epsilon values and an artificial hard stop at $Z > 30$ dBZ associated with high epsilon. Conversations

with the 2A25 algorithm developer indicate that this hard stop at high epsilon was hard coded

in V7.

Fig. 21 - Attenuation corrected stratiform near-surface reflectivity and rain rate data from TRMM 2A25 (a) V6 and (b) V7 algorithm for College Station and Alvin Texas. The colors indicate the value of epsilon for each data point, which is used in the attenuation correction process and has a nominal value of 1.0. The white dashed lines indicate the area between the disdrometer mean rain rate from Fig. 19 +/- the standard deviation for every 1 dBZ of reflectivity.
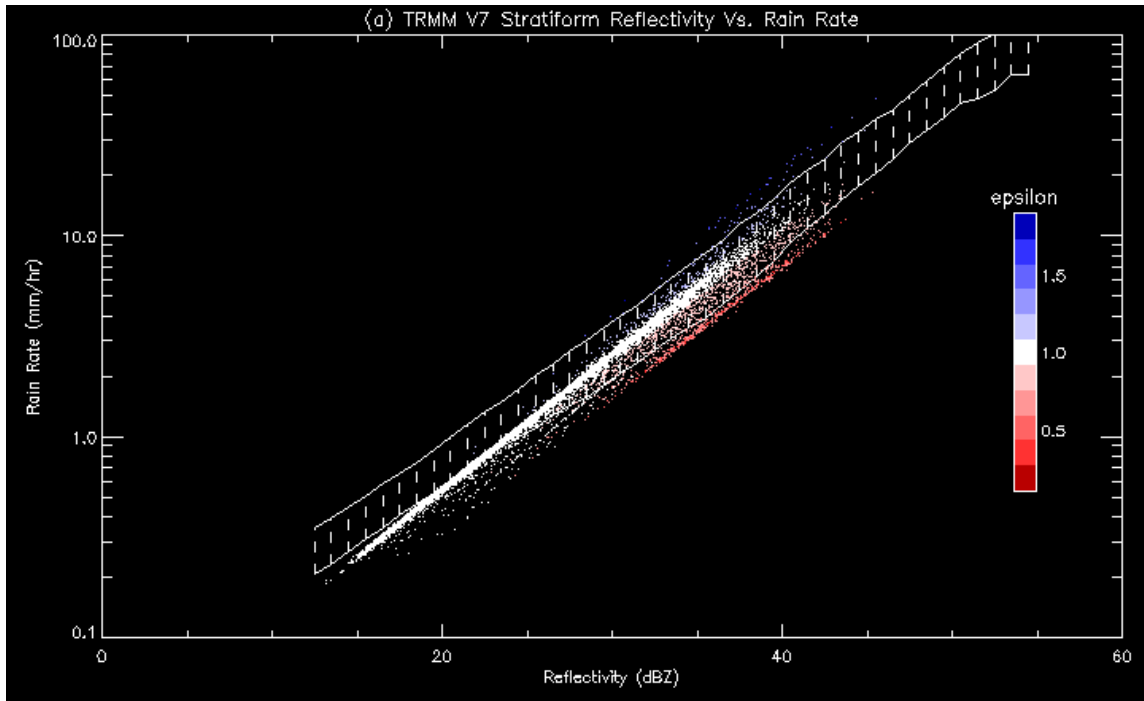
Fig. 21 - Continued

As with the stratiform points in Fig. 21, most of the convective points with epsilon near values of 1 fall within the disdrometer spread, while extreme epsilon values are more likely to fall outside the disdrometer spread (Fig. 22). Unlike the PR stratiform distribution, PR convective points at values of low reflectivity are captured by the disdrometer climatology and V7 brings the higher reflectivity convective points closer to the lower bound of the disdrometer standard deviation. 2A25 V7 attempted to correct an issue of reduced rainfall seen over land, especially in tropical areas such as West Africa and South America. V7 appears to have made some strides in this regard over southeast Texas and is consistent with the work of Kirstetter et al. (2013). However, the hard stop forced by the high epsilon values remains somewhat unnatural and should be considered when analyzing high intensity rain events.

To briefly show the impact of the DSD retrievals on rain rate distributions, Fig. 23 shows a comparison of the frequency of rain rates measured by the disdrometers and retrieved by 2A25 V6 and V7. The TRMM PR sees higher frequencies of rain rates between 0.5 and 10 mm/hr compared to the disdrometers (Fig. 23a). However, the disdrometers see higher frequencies of rain rates > 10 mm/hr (Fig. 23b). Again, this is in line with the findings of Kirstetter et al. (2013) and their study over the southern CONUS. These differences have implications for quantifying intense rain events across the tropics and subtropics, including flash flooding.
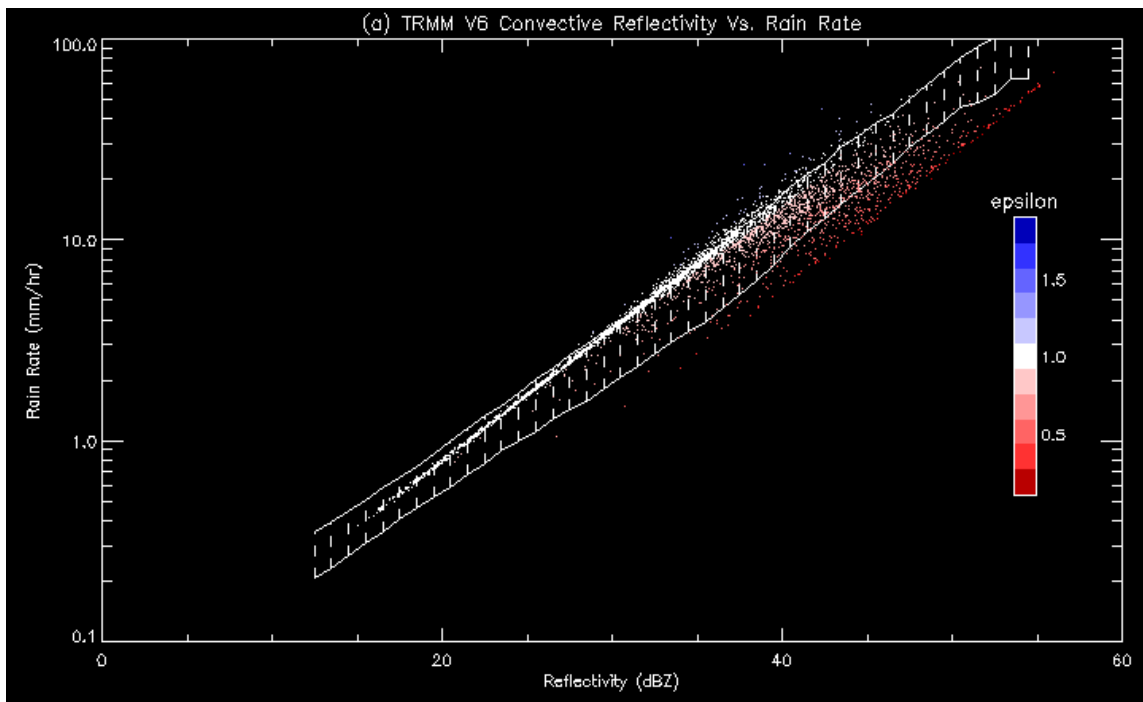
Fig. 22 - Attenuation corrected convective near-surface reflectivity and rain rate data from TRMM 2A25 (a) V6 and (b) V7 algorithm for College Station and Alvin Texas. The colors indicate the value of epsilon for each data point, which is used in the attenuation correction process and has a nominal value of 1.0. The white dashed lines indicate the area between the disdrometer mean rain rate from Fig. 19 +/- the standard deviation for every 1 dBZ of reflectivity.
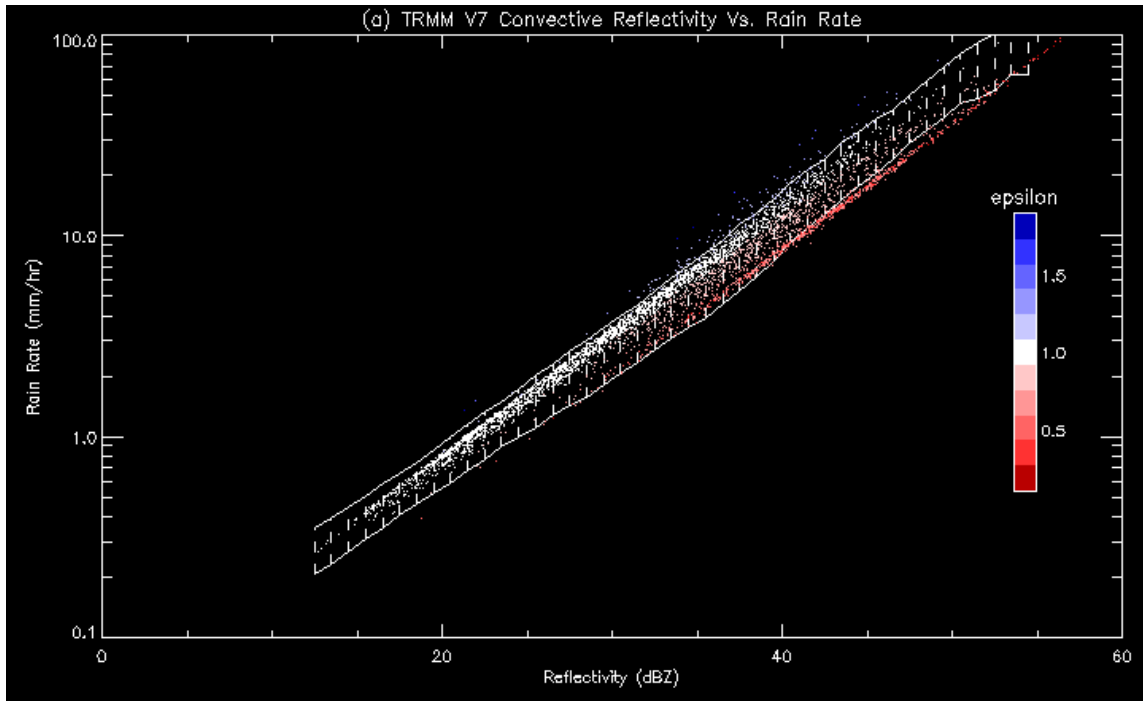
Fig. 22 - Continued
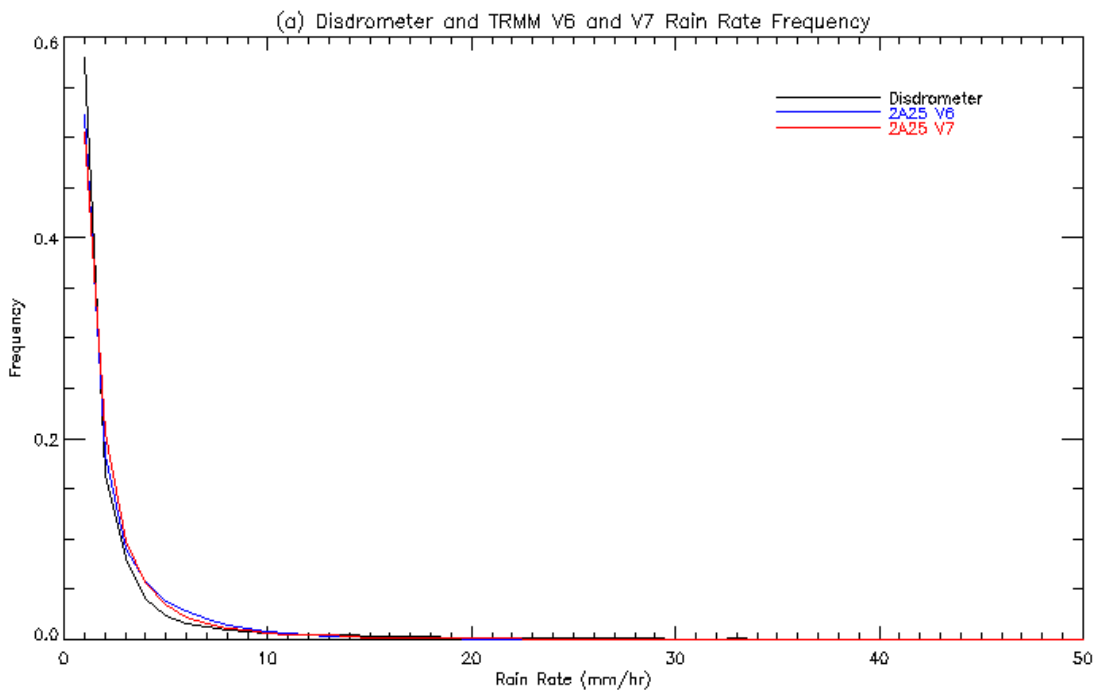
Fig. 23 – Frequency of rain rates for disdrometer, 2A25 V6 and 2A25 V7 for reflectivity values greater than 12 dBZ and (a) all rain rates and (b) rain rates >= 10.

(b) Disdrometer and TRMM V6 and V7 Rain Rate Frequency
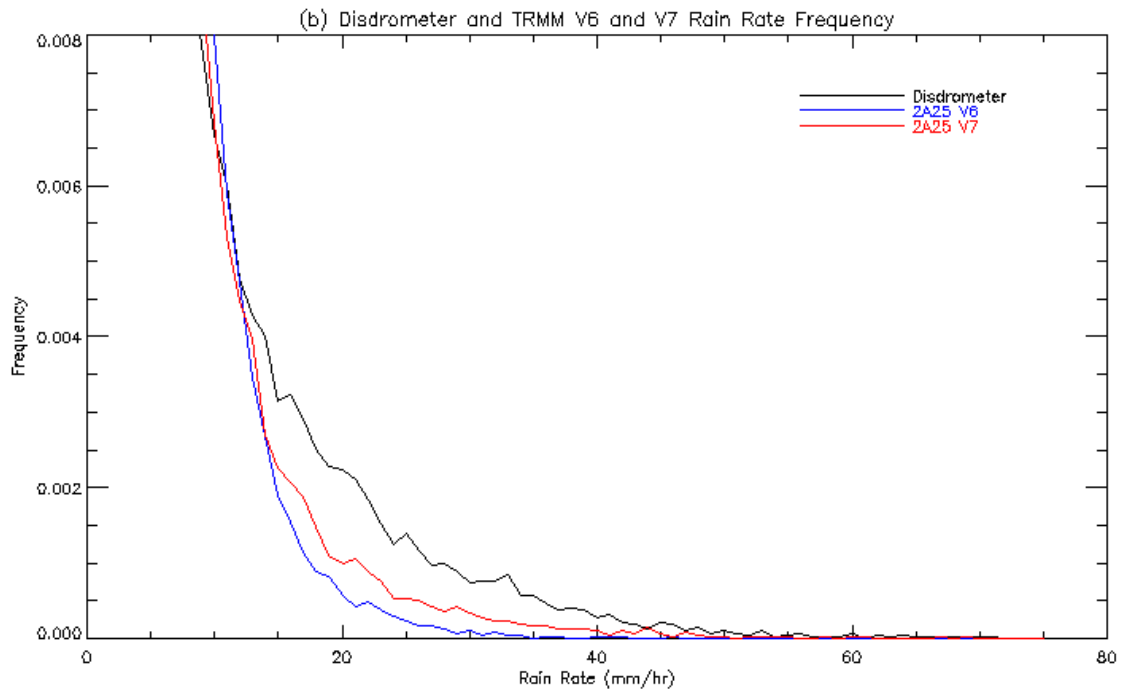
Fig. 23 – Continued

5. CONCLUSION

The continued refinement of the TRMM PR 2A23 algorithm is evidenced by the introduction of new rain types with physically unique properties in V7. The stratiform rain fraction has decreased as a whole over the tropics (20°N-20°S) owing to this refinement, from 40% in V5 to 35%-38% in V7 depending on final convective classifications. While a 2-5% change in overall stratiform fraction may seem small, much larger regional variations are evident across the tropics and impact horizontal and vertical gradients in latent heating, which ultimately alter large-scale circulations (Schumacher et al. 2004). Final convective classifications of 2A23 types by the data user can be informed by the analysis of vertical distributions of reflectivity through FADs, which provide insight into the microphysical and dynamical processes associated with each rain type. FADs of types 140 and 152 suggest that warm-rain processes are at work at lower levels where collision-coalescence is the dominant drop growth mechanism, which would require that the pixels be classified as convective. At upper levels, occurrences of type 140 pixels over the Tibetan Plateau peak during the boreal summer, when most rain is produced by convection; such pixels may have been misclassified as stratiform rain in previous versions of the 2A23 algorithm.

The new concepts of small rain cells and "randomly" appearing shallow non-isolated pixels in 2A23 V7 have moved more echo out of stratiform types into convective types compared with previous versions. These new concepts have likely helped to increase the accuracy of pixel classification in areas such as the Tibetan Plateau and over the oceanic ITCZs. The 2A23 data user can continue these trends by applying the suggested type reclassifications but may wish to consider factors such as the instantaneous nature of 2A23 classifications, the geographical location, and the time of year before doing so. Overall, the

2A23 rain types show continuing promise in their ability to highlight important physical processes in tropical convection. For example, further analysis of the shallow non-isolated population in the eastern Pacific Ocean may indicate important links to the observed shallow meridional circulation (Zhang et al. 2004) and the interannual variability associated with the El Niño-Southern Oscillation.

Rainfall data was collected at two ground sites in southeast Texas from 2004 to 2013. Reflectivity and rain rate values were calculated from DSD data collected by impact disdrometers and organized into rain events. Comparisons of the TRMM PR 2A25 output with the ground-based DSD data reveals that V7 near-surface data compares more favorably with the disdrometer-derived rainfall parameters than V6 and this is particularly true for the TRMM convective rain observations. However, the TRMM PR appears to still underestimate rain at higher values of reflectivity compared to the disdrometer climatology due to an overreliance on the epsilon parameter. Biases in the distribution of TRMM rain rates could have implications for model evaluation, for example, where TRMM rain rate data could be used to evaluate the performance of weather models that are important for predicting events such as flash floods. In addition, regional and global climate models generally see too much light rain and not enough heavy rain. It is important to provide the best observational target in model improvement for both weather and climate applications.

REFERENCES

Awaka, J., T. Iguchi, H. Kumagai, and K. Okamoto, 1997: Rain Type Classification Algorithm for TRMM Precipitation Radar. *Geoscience and Remote Sensing Symposium (IGARSS), 1997 IEEE International*, Singapore, 1633-1635.

Awaka, J., T. Iguchi , and K. Okamoto, 2007: *Rain Type Classification Algorithm. Measuring Precipitation from Space. EURAINAST and the Future*. Dordrecht, Netherlands: Springer, 213-224.

Awaka, J., T. Iguchi , and K. Okamoto, 2009: TRMM PR Standard Algorithm 2A23 and Its Performance on Bright Band Detection. *J. Meteor. Soc. Japan*, **87**, 31-52.

Battan, L. J., 1973: *Radar Observation of the Atmosphere*. Chicago, USA: University of Chicago Press, 324.

Boccippio, D. J., W. A. Petersen, and D. J. Cecil, 2005: The Tropical Convective Spectrum. Part I: Archetypal Vertical Structure. *J. Climate*, **18**, 2744-2769.

Cetrone, J., and R. A. Houze, Jr., 2011: Leading and Trailing Anvil Clouds of West African Squall Lines. *J. Atmos. Sci.*, **68**, 1114-1123.

Fu, Y., and G. Liu, 2007: Possible Misidentification of Rain Type by TRMM PR over Tibetan Plateau. *J. Appl. Meteor. Climatol.*, **46**, 667-672.

Fujinami, H., and T. Yasunari, 2001: The Seasonal and Intraseasonal Variability of Diurnal Cloud Activity over the Tibetan Plateau. *J. Meteor. Soc. Japan*, **79**, 1207-1227.

Funk, A., C. Schumacher, and J. Awaka, 2013: Analysis of Rain Classifications over the Tropics by Version 7 of the TRMM PR 2A23 Algorithm. *J. Meteor. Soc. Japan*, **91**, 257-272.

Futyan, J. M., and A. D. Del Genio, 2007: Deep Convective System Evolution over Africa and the Tropical Atlantic. *J. Climate*, **20**, 5041-5060.

Hartmann, D. L., H. H. Hendon, and R. A. Houze, Jr., 1984: Some Implications of the Mesoscale Circulations in Tropical Cloud Clusters for Large-scale Dynamics and Climate. *J. Atmos. Sci.*, **41**, 113-121.

Hitschfeld, W., and J. Bordan, 1954: Errors Inherent in the Radar Measurement of Rainfall at Attenuating Wavelengths. *J. Meteor.*, **11**, 58-67.

Houze, R. A., Jr., 1997: Stratiform Precipitation in Regions of Convection: A Meteorological Paradox? *Bull. Amer. Meteor. Soc.*, **78**, 2179-2196.

Houze, R. A., Jr., 1982: Cloud Clusters and Large-scale Vertical Motions in the Tropics. *J. Meteor. Soc. Japan*, **60**, 396-410.

Iguchi, T., T. Kozu, J. Kwiatkwoski, R. Meneghini, J. Awaka, and K. Okamoto, 2009: Uncertainties in the Rain Profiling Algorithm for the TRMM Precipitation Radar. *J. Meteor. Soc. Japan*, **87A**, 1-30.

Iguchi, T., T. Kozu, R. Meneghini, J. Awaka, and K. Okamoto, 2000: Rain-profiling Algorithm for the TRMM Precipitation Radar. *J. Appl. Meteor.*, **39**, 2038-2052.

Islam, M. N., and H. Uyedam, 2007: Use of TRMM in Determining the Climatic Characteristics of Rainfall over Bangladesh. *Remote Sens. Environ,*, **108**, 264-276.

Joss, J. and A. Waldvogel, 1967: Ein Spektrograph Fur Niederschlagstropfen mit automatischer Auswertung (A Spectrograph for Rain Drops with Automatical Analysis). *Pure Appl. Geophys.*, **68**, 240-246.

Kelley, O. A., J. Stout, M. Summers, and E. J. Zipser, 2010: Do the Tallest Convective Cells Over the Tropical Ocean Have Slow Updrafts? *Mon. Wea. Rev.*, **138**, 1651-1672.

Kirstetter, P., Y. Hong, J. J. Gourley, M. Schwaller, W. Petersen, and J. Zhang, 2013: Comparison of TRMM 2A25 Products, Version 6 and Version 7, with NOAA/NSSL Ground Radar-Based National Mosaic QPE. *J. Hydrometeor.*, **14**, 661-669.

Kozu, T., T. Iguchi, T. Kubota, N. Yoshida, S. Seto, J. Kwiatkowski, and Y. N. Takayabu, 2009a: Feasibility of Raindrop Size Distribution Parameter Estimation with TRMM Precipitation Radar. *J. Meteor. Soc. Japan*, **87A**, 53-66.

--, --, T. Shimomai, and N. Kashiwagi, 2009b: Raindrop Size Distribution Modeling from a Statistical Rain Parameter Relation and Its Application to the TRMM Precipitation Radar Rain Retrieval Algorithm. *J. Appl. Meteoro. Climotol.*, **48**, 716-724.

Kummerow, C., W. Barnes, T. Kozu, J. Shiue, and J. Simpson, 1998: The Tropical Rainfall Measuring Mission (TRMM) Sensor Package. *J. Atmos. Oceanic Technol.*, **15**, 809-817.

Kuettner, J. P., 1974: General Description and Central Program of GATE. *B. Am. Meteorol. Soc.*, **55**, 712-719.

Leary, C. A., and R. A. Houze Jr., 1979: Melting and Evaporation of Hydrometeors in Precipitation from the Anvil Clouds of Deep Tropical Convection. *J. Atmos. Sci*, **36**, 437-457.

Li, W., and C. Schumacher, 2011: Thick Anvils as Viewed by the TRMM Precipitation Radar. *J. Climate*, **24**, 1718-1735.

Marshall, J. S., and W. McK. Palmer, 1948: The Distribution of Raindrops with Size., *J. Meteor.*, **5**, 165-166.

Meneghini, R., J. Eckerman, and D. Atlas, 1983: Determination of Rain Rate from a Spaceborne Radar Using Measurements of Total Attenuation. *IEEE Trans. Geosci. Remote Sens.*, **21**, 34-43.

Meneghini, R., T. Iguchi, T. Kozu, L. Liao, K. Okamoto, J. A. Jones, and J. Kwiatkowski, 2000: Use of the Surface Reference Technique for Path Attenuation Estimates from the TRMM Precipitation Radar. *J. Appl. Meteor.*, **39**, 2053-2070.

Rasmussen, K. L., S. L. Choi, M. D. Zuluaga, and R. A. Houze, Jr., 2013: TRMM Precipitation Bias in Extreme Storms in South America. *Geophys. Res. Lett.*, **40**, 3457-3461.

Schumacher, C., and R. A. Houze, Jr., 2003a: The TRMM Precipitation Radar's View of Shallow, Isolated Rain. *J. Appl. Meteor.*, **42**, 1519-1524.

Schumacher, C., and R. A. Houze, Jr., 2003b: Stratiform Rain in the Tropics as Seen by the TRMM Precipitation radar. *J. Climate*, **16**, 1739-1756.

Schumacher, C., and R. A. Houze, Jr., 2006: Stratiform Precipitation Production over Sub-Saharan Africa and the Tropical East Atlantic as Observed by TRMM. *Quart. J. Roy. Meteor. Soc.*, **132**, 2235-2255.

Schumacher, C., R. A. Houze, Jr., and I. Kraucunas, 2004: The Tropical Dynamical Response to Latent Heating Estimates Derived from the TRMM Precipitation Radar. *J. Atmos. Sci.*, **61**, 1341-1358.

Seto, S., T. Iguchi, and R. Meneghini, 2011: Comparison of TRMM PR V6 and V7 Focusing Heavy Rainfall. *Geoscience and Remote Sensing Symposium (IGARSS), 2011 IEEE International*, Vancouver, BC, 2582-2585.

Shige, S., Y. N. Takayabu, and W.-K. Tao, 2008: Spectral Retrieval of Latent Heating Profiles from TRMM PR Data. Part III: Estimating Apparent Moisture Sink Profiles over Tropical Oceans. *J. Appl. Meteor. Climatol.*, **47**, 620-640.

Shige, S., Y. N. Takayabu, W.-K. Tao, and C.-L. Shie, 2007: Spectral Retrieval of Latent Heating Profiles from TRMM PR Data. Part II: Algorithm Improvement and Heating Estimates over Tropical Ocean Regions. *J. Appl. Meteor. Climatol.*, **46**, 1098-1124.

Shige, S., Y. N. Takayabu, W.-K. Tao, and D. E. Johnson, 2004: Spectral Retrieval of Latent Heating Profiles from TRMM PR Data. Part I: Development of a Model-based Algorithm. *J. Appl. Meteor.*, **43**, 1095-1113.

Shimizu, S., R. Oki, T. Tagawa, T. Iguchi, and M. Hirose, 2009: Evaluation of the Effects of the Orbit Boost of the TRMM Satellite on PR Rain Estimates. *J. Meteor. Soc. Japan*, **87A**, 83-92.

Short, D., and K. Nakamura, 2000: TRMM Radar Observations of Shallow Precipitation over the Tropical Oceans. *J. Climate*, **13**, 4107-4124.

Simpson, J., R. F. Adler, and G. R. North, 1988: A Proposed Tropical Rainfall Measuring Mission (TRMM) Satellite. *B. Am. Meteorol. Soc.*, **69**, 278-295.

Smith, P. L., Z. Liu, and J. Joss, 1993: A Study of Sampling-Variability Effects in Raindrop Size Observations. *J. Appl. Meteor.*, **32**, 1259-1269.

Steiner, M., R. A. Houze, Jr., and S. E. Yuter, 1995: Climatological Characterization of Three-dimensional Storm Structure from Operational Radar and Rain Gauge Data. *J. Appl. Meteor.*, **34**, 1978-2007.

Steiner, M., and J. A. Smith, 2000: Reflectivity Rain Rate and Kinetic Energy Flux Relationships Based on Raindrop Spectra. *J. Appl. Meteor.*, **39**, 1923-1940.

Tokay, A. D., and D. A. Short, 1996: Evidence from Tropical Raindrop Spectra of the Origin of Rain from Stratiform versus Convective Clouds. *J. Appl. Meteor.*, **35**, 355-371.

Tokay, A., D. B. Wolff, K. R. Wolff, and P. Bashor, 2003: Rain Gauge and Disdrometer Measurements during the Keys Area Microphysics Project (KAMP). *J. Atmos. Oceanic Technol.*, **20**, 1460-1477.

TRMM PR Team, 2011: *Tropical Rainfall Measuring Mission (TRMM) precipitation radar algorithm Instruction Manual for Version 7*. JAXA-NASA, 170 pp. [Available online at http://www.eorc.jaxa.jp/TRMM/documents/PR_algorithm_product_information/pr_manual/PR_Instruction_Manual_V7_L1.pdf.]

Yuter, S., and R. A. Houze, Jr., 1995: Three-dimensional Kinematic and Microphysical Evolution of Florida Cumulonimbus. Part II: Frequency Distributions of Vertical Velocity, Reflectivity, and Differential Reflectivity. *Mon. Wea. Rev.*, **123**, 1941-1963.

Yuter, S. E., and R. A. Houze, Jr., 1997: Measurements of Raindrop Size Distribution Over the Pacific Warm Pool and Implications for Z-R Relations. *J. Appl. Meteor.*, **36**, 847-867.

Zhang, C., and S. M. Hagos, 2009: Bi-modal Structure and Variability of Large-scale Diabatic Heating in the Tropics. *J. Atmos. Sci.*, **66**, 3621-3640.

Zhang, C., M. McGauley, and N. A. Bond, 2004: Shallow Meridional Circulation in the Tropical Eastern Pacific. *J. Climate*, **17**, 133-139.